

AD-A130 194

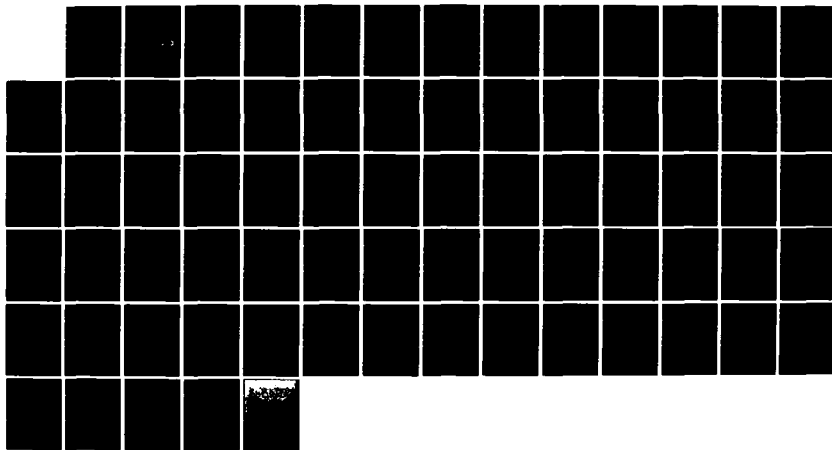
COMPUTATION OF THREE-DIMENSIONAL FLOWS IN DUCTS OF
VARYING CROSS SECTIONS(U) MINNESOTA UNIV MINNEAPOLIS
DEPT OF MECHANICAL ENGINEERING S V PATANKAR MAY 83
N00014-81-K-0555

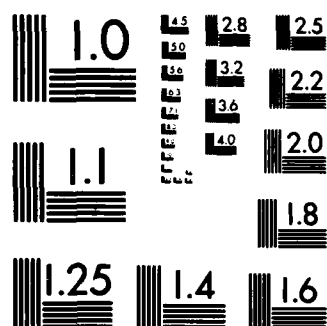
1/1

UNCLASSIFIED

F/G 12/1

NL





MICROCOPY RESOLUTION TEST CHART
NATIONAL BUREAU OF STANDARDS-1963-A

ADA 136

(12)

First Summary Report
Contract N00014-81-K-05555; NR 097-452

COMPUTATION OF THREE-DIMENSIONAL FLOWS IN DUCTS OF VARYING CROSS SECTIONS

Suhas V. Patankar
Department of Mechanical Engineering
University of Minnesota
Minneapolis, MN 55455

May 1983

DTIC
ELECTE
JUL 7 1983
S A D

Period: June 15, 1981 to January 15, 1983

This document has been approved
for public release and sale; its
distribution is unlimited.

Prepared for
Office of Naval Research
800 North Quincy Street
Arlington, VA 22217

DTIC FILE COPY

First Summary Report
Contract N00014-81-K-05555; NR 097-452

COMPUTATION OF THREE-DIMENSIONAL FLOWS IN DUCTS OF VARYING CROSS SECTIONS

Suhas V. Patankar
Department of Mechanical Engineering
University of Minnesota
Minneapolis, MN 55455

May 1983

Period: June 15, 1981 to January 15, 1983

Prepared for
Office of Naval Research
800 North Quincy Street
Arlington, VA 22217

Unclassified

SECURITY CLASSIFICATION OF THIS PAGE (When Data Entered)

REPORT DOCUMENTATION PAGE		READ INSTRUCTIONS BEFORE COMPLETING FORM
1. REPORT NUMBER N00014-81-K-0555-1983-1	2. GOVT ACCESSION NO. AD-A130194	3. RECIPIENT'S CATALOG NUMBER
4. TITLE (and Subtitle) COMPUTATION OF THREE-DIMENSIONAL FLOWS IN DUCTS OF VARYING CROSS SECTIONS		5. TYPE OF REPORT & PERIOD COVERED Summary Report June 15, 1981 to Jan. 15, 1983
		6. PERFORMING ORG. REPORT NUMBER
7. AUTHOR(s) Suhas V. Patankar		8. CONTRACT OR GRANT NUMBER(s) N00014-81-K-0555
9. PERFORMING ORGANIZATION NAME AND ADDRESS Department of Mechanical Engineering University of Minnesota, 111 Church St. S.E., Minneapolis, MN 55455		10. PROGRAM ELEMENT, PROJECT, TASK AREA & WORK UNIT NUMBERS Work unit NR 097-452
11. CONTROLLING OFFICE NAME AND ADDRESS Office of Naval Research 800 North Quincy Street Arlington, Virginia 22217		12. REPORT DATE May 1983
		13. NUMBER OF PAGES 62
14. MONITORING AGENCY NAME & ADDRESS (if different from Controlling Office)		15. SECURITY CLASS. (of this report) Unclassified
		15a. DECLASSIFICATION/DOWNGRADING SCHEDULE
16. DISTRIBUTION STATEMENT (of this Report) Approved for public release; distribution unlimited.		
17. DISTRIBUTION STATEMENT (of the abstract entered in Block 20, if different from Report)		
18. SUPPLEMENTARY NOTES		
19. KEY WORDS (Continue on reverse side if necessary and identify by block number) Fluid flow, numerical methods, duct flow.		
20. ABSTRACT (Continue on reverse side if necessary and identify by block number) A calculation procedure is developed for the three-dimensional flow in ducts of varying cross section. The procedure is of the fully parabolic variety; i.e., the solution for the whole duct is obtained by a marching scheme that proceeds from the upstream end to the downstream region solving the flow over one cross section at each marching step. The procedure for each cross section is based on the finite element method of Baliga and Patankar. The report describes a major improvement incorporated in the method and some examples of the use of the method.		

DD FORM 1473

1 JAN 73

EDITION OF 1 NOV 68 IS OBSOLETE
S/N 0102-LF-014-6601

Unclassified

SECURITY CLASSIFICATION OF THIS PAGE (When Data Entered)

Unclassified

SECURITY CLASSIFICATION OF THIS PAGE (When Data Entered)

The adaptation of the method for a marching procedure for duct flows is also described. Among the examples presented as test problems are the developing flows: in a square duct, over a rod bundle, in a square diffuser, and in an elliptic duct of varying cross-sectional shape. All numerical solutions are shown to be in satisfactory agreement with exact solutions and/or other available solutions and experimental data.

Accession For	
DTIC	<input checked="checked" type="checkbox"/>
NTIS	<input type="checkbox"/>
Unannounced	<input type="checkbox"/>
Classification	
Distribution/	
Availability Codes	
Avail and/or	Special
Dist	A

DTIC
COPY
INSPECTED
2

Unclassified

SECURITY CLASSIFICATION OF THIS PAGE (When Data Entered)

CONTENTS

	Page
1. Introduction	1
2. Method for two-dimensional flows	3
2.1 Governing differential equation	3
2.2 Domain discretization	3
2.3 Discretization equation	4
2.4 Solution of the discretization equations	5
2.5 Calculation of fluid flow	6
2.6 Discretized momentum equations	7
2.7 Treatment of the continuity equation	8
2.8 The overall solution procedure	10
3. Application of the method to some two-dimensional problems	12
3.1 Flow between two concentric rotating cylinders	12
3.2 The driven cavity problem	18
3.3 Natural convection in a square cavity	23
4. Method for three-dimensional duct flows	33
4.1 Governing differential equation	33
4.2 Domain discretization	34
4.3 Discretization equation	36
4.4 Calculation of the overall pressure gradient	37
4.5 The overall solution procedure	38
5. Application of the method to some three-dimensional duct flows	40
5.1 Flow through ducts of uniform cross section	40
5.1-1 Developing flow in a square duct	40
5.1-2 Developing flow over rod bundles	42
5.2 Flow through ducts of varying cross-sectional shape and area	47
5.2-1 Formulation of the exact solutions	47
5.2-2 Flow through a square diffuser	52
5.2-3 Flow through an elliptic duct	54
6. Concluding remarks	58
References	62

1. Introduction

Duct flows occur in a variety of engineering applications. They are present in aircraft and automobile engines, heat exchangers, steam generators, and piping systems. Often, the ducts have a noncircular cross section, which undergoes a change of shape and size along the length of the duct. The purpose of the present research project is to develop a calculation procedure for the prediction of flow in such ducts.

Many duct flows are characterized by the absence of reverse flow or separation and by a nearly uniform pressure over any cross section. These conditions are found when the change in the size and shape of the cross section is gradual rather than sudden. Such flows can be treated as fully parabolic, i.e., they can be predicted by a marching procedure starting at the inlet plane and proceeding to successive cross-sectional planes downstream. The procedure described in this report is of the fully parabolic variety.

If significant pressure variations arise over a cross section, they can be incorporated in a procedure known as partially parabolic. In such a procedure, the duct length must be swept many times by the marching calculation until the three-dimensional pressure variations are properly established and used in the flow calculation. If a reverse flow is present in the duct, a fully elliptic procedure is needed for its calculation.

The fully parabolic procedure employed in this report calculates the flow over one cross section at a time. Thus, the computational task is almost the same as solving a two-dimensional problem over a domain of arbitrary shape. The method of Baliga and Patankar [1, 2] was chosen to be the starting point for this purpose. In the course of adapting that method, an improvement in the treatment of pressure was worked out. The two-dimensional calculation scheme along with the proposed improvement is described in Section 2 of this report. The method has been tested

on a large number of problems to evaluate its correctness, accuracy, convergence, and other behavior. Results of some of the test problems are presented in Section 3.

The extension of the two-dimensional method to three-dimensional duct flows is described in Section 4. Section 5 is devoted to some applications of the method. They include the developing flow in some constant-area ducts; but of particular importance are the calculations for two ducts of varying cross-sectional area and shape.

2. Method for two-dimensional flows

When a three-dimensional duct flow is treated as fully parabolic in nature, its calculation is performed by a marching procedure in the main flow direction. At each marching station, a computationally two-dimensional problem is solved over the duct cross section. Thus, a procedure for two-dimensional flows forms an essential building block of the method for three-dimensional parabolic flows. The two-dimensional procedure employed in the present work is described in this section.

It was intended to employ the two-dimensional finite-element procedure of Baliga and Patankar [1, 2] for this building block. However, the treatment of the pressure field in [2] is somewhat inconvenient; therefore, an improved treatment was worked out. It is this improved procedure that is described here.

2.1 Governing differential equation

As described in [3], the fluid flow and heat transfer phenomena in steady state are governed by a general differential equation of the form:

$$\frac{\partial}{\partial x_j} (\rho u_j \phi) = \frac{\partial}{\partial x_j} \left(\Gamma \frac{\partial \phi}{\partial x_j} \right) + S \quad (2.1)$$

where ϕ is the general dependent variable, ρu_j denotes the mass flow rate causing the convective transport, Γ is the diffusion coefficient, and S represents the source term. The variable ϕ can stand for enthalpy (or temperature), concentration, turbulence energy, or a velocity component. Thus, a solution procedure for any convective phenomenon should provide a mechanism for solving Eq. (2.1).

2.2 Domain discretization

In the calculation procedure described in [1, 2], the physical domain of interest is discretized into triangular elements as shown in Fig. 2.1. The vertices of the triangles are called nodes or grid points. The aim of the calculation scheme is to obtain the values of ϕ at these nodes.

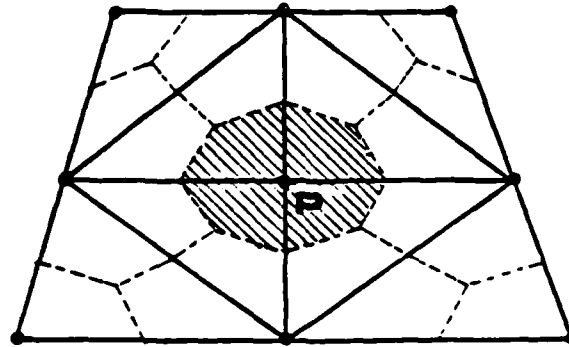


Fig. 2.1 Domain discretization

The algebraic equations for the ϕ values at the nodes are obtained by integrating Eq. (2.1) over the polygonal control volume associated with each node. The construction of these control volumes is also shown in Fig. 2.1. Each triangular element is split into three parts by joining its centroid to the centers of the three sides. The control volume around a typical node P is composed of the parts of all the neighboring triangles that contain the point P.

2.3 Discretization equation

The discretization form of Eq. (2.1) is obtained by integrating the differential equation over a control volume. Such integral equation consists of the total source term S over the control volume and the net convection and diffusion flux across the faces of the control volume. As seen from Fig. 2.1, the control-volume faces are composed of the dashed lines that lie within each triangle. To express the total flux (i.e., the convection flux plus the diffusion flux) across such a dashed line in terms of the nodal values of ϕ , a shape function is required.

As explained in [1], an appropriate shape function for convection-diffusion problems is one that takes account of the resultant flow direction. The shape

function suggested in [1] and implemented in this work is

$$\phi = A + B \exp(\rho UX/\Gamma) + CY \quad (2.2)$$

where, as shown in Fig. 2.2, the coordinate X is aligned in the resultant flow direction, while Y is taken as normal to it. The quantity U represents the magnitude of the velocity vector. The constants A, B, and C in Eq. (2.2) are expressible in terms of ϕ_1 , ϕ_2 , ϕ_3 at the three nodes of the triangle.

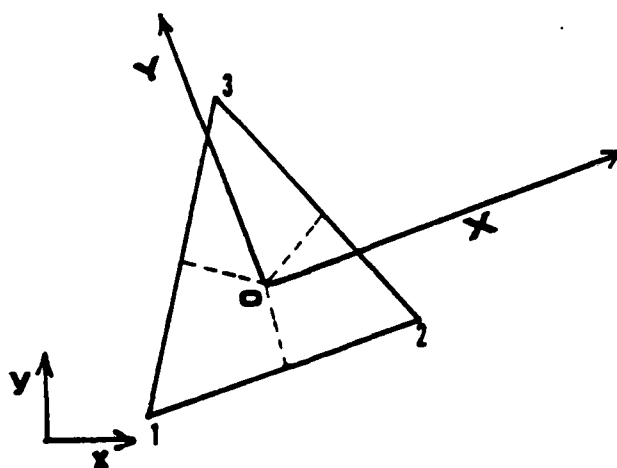


Fig. 2.2 Coordinate axes for shape function

The use of Eq. (2.2) in the integral equation for the control volume leads to the algebraic equation

$$a_p \phi_p = \sum_{nb} a_{nb} \phi_{nb} + b \quad (2.3)$$

where the subscript nb denotes a neighbor node of P and the summation is taken over all the neighbors of P. The coefficients a_p and a_{nb} represent the convection-diffusion influence, while b contains the integral of the source term S over the control volume.

2.4 Solution of the discretization equations

The algebraic equations such as (2.3) form a set of linear simultaneous equations. They can be solved by a variety of methods. In the computer implementation

of the proposed method, the domain discretization is performed by the use of a line structure. Although this places some restriction on the shape of the domain or on the local grid fineness, the technique provides considerable convenience in node numbering and in the solution of equations. With the nodes arranged on a line pattern, the line-by-line method [3] becomes the natural choice for solving the algebraic equations. It is this method that is employed in the present work.

2.5 Calculation of fluid flow

Although the general dependent variable ϕ can stand for the two velocity components u and v in a two-dimensional flow and thus a calculation procedure for fluid flow is contained within the general procedure for solving Eq. (2.1), there is an important complication. The source term S contains the pressure gradient $\partial p / \partial x$ or $\partial p / \partial y$ when ϕ stands for u or v . The pressure field p represents an extra degree of freedom and it is indirectly constrained by the requirement that the velocity field must satisfy the continuity equation

$$\frac{\partial}{\partial x_j} (\rho u_j) = 0 \quad (2.4)$$

The combined treatment of the momentum and continuity equations forms the special features of a fluid-flow calculation.

If the velocity components and pressure are stored at the same grid points, then the required interpolations of pressure and velocity lead to discretization equations that admit unrealistic zig-zag velocity fields and checkerboard pressure fields. This is explained at length in [3]. The remedy adopted in finite-difference methods is a staggered grid, in which the velocity components are stored at locations that are displaced (or staggered) relative to the pressure nodes. The same remedy is not available in finite element methods, since the lines joining adjacent nodes do not lie along the coordinate directions. The common remedy is a mixed-interpolation (or unequal-order) scheme, in which pressure is stored at fewer locations

than the velocity components. This practice is employed in [2] and also by earlier workers.

Although the unequal-order procedure is adequate, it is not entirely satisfactory. It leads to complications in numbering sequences, control-volume definitions, etc., since the pressure grid and the velocity grid must be handled separately. Moreover, the coarser grid used for pressure would limit the accuracy of the solution. If the pressure grid is made sufficiently fine, the associated velocity grid becomes excessively fine and thus wasteful. In the interests of convenience and efficiency, an equal-order procedure is thus sought.

2.6 Discretized momentum equations

Since the momentum equations are special cases of the general differential equation (2.1), they can be cast into the discretization form similar to Eq. (2.3).

Thus

$$a_p u_p = \sum a_{nb} u_{nb} + b^u \quad (2.5)$$

$$a_p v_p = \sum a_{nb} v_{nb} + b^v \quad (2.6)$$

where b^u and b^v are the integrals (over of the control volume) of the source terms

$$(S^u - \partial p / \partial x) \quad \text{and} \quad (S^v - \partial p / \partial y)$$

respectively.

For further rearrangement of the equations, pseudovelocities \hat{u} and \hat{v} are defined by

$$\hat{u}_p = (\sum a_{nb} u_{nb}) / a_p \quad (2.7)$$

and

$$\hat{v}_p = (\sum a_{nb} v_{nb}) / a_p \quad (2.8)$$

Then the momentum equations (2.5) and (2.6) can be rewritten as

$$u_p = \hat{u}_p + d^u (S^u - \partial p / \partial x)_{c.v.} \quad (2.9)$$

and

$$v_p = \hat{v}_p + d^v (S^v - \partial p / \partial y)_{c.v.} \quad (2.10)$$

where the subscript c.v. indicates an average value over the control volume. The multipliers d^u and d^v can be seen to be

$$d^u = d^v = \Delta V / a_p \quad (2.11)$$

where ΔV is the volume of the control volume.

No novelty has yet been introduced. If, in the continuity equation, a linear interpolation of u and v is used, the well-known difficulties associated with storing all variables at every node would result. The equal-order procedure here is developed by proposing a different interpolation technique for the continuity equation. This technique is described next.

2.7 Treatment of the continuity equation

The discretized form of Eq. (2.4) would contain mass flow rates across the boundaries of a typical control volume shown in Fig. 2.1. These flow rates can be compiled by calculating the flow crossing the three dashed line segments in every element. A typical element is shown in Fig. 2.3 .

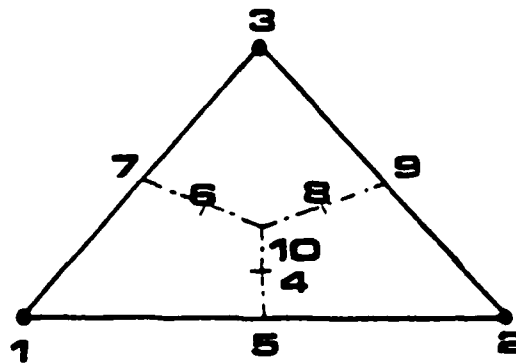


Fig. 2.3 Control-volume faces within an element

Although it is possible to calculate u and v at any point within the element by a linear interpolation between the nodal values of u and v , the practice proposed here makes the velocities appearing in the continuity equation directly responsive to the pressure gradient over the element. Thus, for the purpose of the continuity equation, the velocity field within an element is calculated from \tilde{u} and \tilde{v} , where

$$\tilde{u} = \hat{u} + d^u [S^u - \partial p / \partial x]_e \quad (2.12)$$

$$\tilde{v} = \hat{v} + d^v [S^v - \partial p / \partial y]_e \quad (2.13)$$

where the subscript e indicates the element under consideration. The source terms S^u and S^v are considered to be uniform over an element. Further, if the pressure p is described by a linear shape function over the element, the gradients $\partial p / \partial x$ and $\partial p / \partial y$ also become uniform. The calculation of \hat{u} , \hat{v} , d^u , and d^v at the nodes has been outlined in Eqs. (2.7), (2.8), and (2.11). For the calculation of \tilde{u} and \tilde{v} from Eqs. (2.12)-(2.13), the values of \hat{u} , \hat{v} , d^u , and d^v are considered to vary linearly over the element. As a result, the \tilde{u} and \tilde{v} values would have a linear distribution.

That the \tilde{u} and \tilde{v} field as given by Eqs. (2.12)-(2.13) is "driven" directly by the nodal pressures in a given element is the essential feature of this formulation. This eliminates the possibility of checkerboard pressure fields.

To obtain a discretization equation for pressure, first a discretized form of the continuity equation is written by integrating it over the typical control volume shown in Fig. 2.1. The mass flow rates across the faces of the control volume are expressed in terms of \tilde{u} and \tilde{v} defined in Eqs. (2.12) - (2.13). The pressure gradients $\partial p / \partial x$ and $\partial p / \partial y$ are written in terms of the nodal pressure. The result is the following discretization equation for p , which has the same appearance as Eq. (2.3)

$$a_p p_p = \sum a_{nb} p_{nb} + b \quad (2.14)$$

where P denotes a typical node shown in Fig. 2.1, nb stands for a neighbor node of P , and the summation is taken over all the neighbors. The coefficients a_p and a_{nb} arise from the multipliers d^u and d^v in Eqs. (2.12)-(2.13). The term b in Eq. (2.14) contains \hat{u} , \hat{v} , S^u , and S^v . Since the structure of Eq. (2.14) is identical to that of Eq. (2.3), the line-by-line solution method mentioned in Section 2.4 is applicable to Eq. (2.14) as well.

An alternative form of Eq. (2.14) can be derived by defining a pressure correction p' such that

$$p = p^* + p' \quad (2.15)$$

where p^* is the current estimate or guess for pressure. If the momentum equations (2.5) - (2.6) are solved by substituting the guessed pressure field p^* , the resulting velocities can be denoted by u^* and v^* . Consequently, a velocity field u^* and v^* can be obtained from Eqs. (2.12) - (2.13) by substituting p^* for p and by calculating \hat{u} and \hat{v} from the u^* and v^* values. Then the counterpart of Eq. (2.14) can be written as

$$a_p p'_p = \sum a_{nb} p'_{nb} + b \quad (2.16)$$

where a_p and a_{nb} are identical to the corresponding coefficients in Eq. (2.14) and b results from the substitution of the \tilde{u}^* and \tilde{v}^* field in the continuity equation.

2.8 The overall solution procedure

Since all the ingredients of the calculation procedure have been outlined, the overall procedure can now be described in terms of the various steps in the calculation sequence.

- (1) Start with initial guesses for u , v , \tilde{u} , \tilde{v} , and other relevant variables.
- (2) Calculate the coefficients in the momentum equations for u and v .
- (3) Hence obtain \hat{u} , \hat{v} , d^u , and d^v from Eqs. (2.7), (2.8), and (2.11).
- (4) Set up Eq. (2.14) and solve it to get a pressure field.
- (5) Treating this as p^* , solve the momentum equations to obtain u^* and v^* .

(6) Hence set up the pressure-correction equation (2.16) and solve it. Use the resulting p' values to correct \tilde{u}^* , \tilde{v}^* , u^* and v^* . At this stage, the corrected field \tilde{u} , \tilde{v} would satisfy continuity.

(7) Solve Eq. (2.3) for other relevant dependent variables such as temperature, concentration, turbulence parameters, etc.

(8) Return to step 2 and repeat until convergence.

3. Application of the method to some two-dimensional problems

In this section, the proposed method is applied to three test problems.

3.1 Flow between two concentric rotating cylinders

The flow of an incompressible fluid between two concentric rotating cylinders is shown schematically in Fig. 3.1. The inner cylinder is supposed to be at rest while the outer cylinder rotates with angular velocity ω . In the $(r-\theta)$ polar coordinates, this is a one-dimensional problem with the radial component of velocity u_r being identically zero. However, in the Cartesian coordinates $(x-y)$, the problem is fully two-dimensional, with non-vanishing velocity components u and v along the x and y coordinates respectively. The aim here is to solve this two-dimensional problem in the $x-y$ coordinates over a square region R shown shaded in Fig. 3.1.

The exact solution

Let u_θ , u_r and p be, respectively, the circumferential velocity, the radial velocity and pressure. Also let u and v be the velocity components along the x and y directions. At this point, the following dimensionless variables are introduced.

$$u_\theta^* = \frac{u_\theta}{2r_1\omega} \quad (3.1)$$

$$u_r^* = \frac{u_r}{2r_1\omega} \quad (3.2)$$

$$p^* = \frac{(p-p_0)}{\rho(2r_1\omega)^2} \quad (3.3)$$

$$u^* = \frac{u}{(2r_1\omega)} \quad (3.4)$$

$$v^* = \frac{v}{(2r_1\omega)} \quad (3.5)$$

$$r^* = \frac{r}{r_1} \quad (3.6)$$

$$x^* = \frac{x}{r_1} \quad (3.7)$$

$$y^* = \frac{y}{r_1} \quad (3.8)$$

where, ρ is the fluid density, and p_0 is the reference pressure on inner cylinder ($r=r_1$). For a radius ratio of 2 between the outer and inner cylinders, as shown in Fig. 3.1, the exact solution to the problem is given by

$$u_\theta^* = -\frac{2}{3}(r^* - \frac{1}{r^*}) \quad (3.9)$$

$$u_r^* = 0 \quad (3.10)$$

and

$$p^* = \frac{2}{9}(r^{*2} - \frac{1}{r^{*2}}) - \frac{8}{9} \ln r^* \quad (3.11)$$

from which it follows that

$$u^* = \frac{2}{3}(r^* - \frac{1}{r^*}) \frac{y^*}{r^*} \quad (3.12)$$

and

$$v^* = -\frac{2}{3}(r^* - \frac{1}{r^*}) \frac{x^*}{r^*} \quad (3.13)$$

Domain discretization

Figure 3.2 shows the discretization of the computational domain into quadrilaterals and further subdivision of these quadrilaterals into triangular elements. As can be seen, the uniform $N \times N$ grid has a spacing $\Delta x^* = \Delta y^* = \delta$, where,

$$\delta = \frac{1/\sqrt{2}}{(N-1)} \quad (3.14)$$

Results were obtained for four different grid sizes corresponding to $N = 9, 13, 17$ and 21.

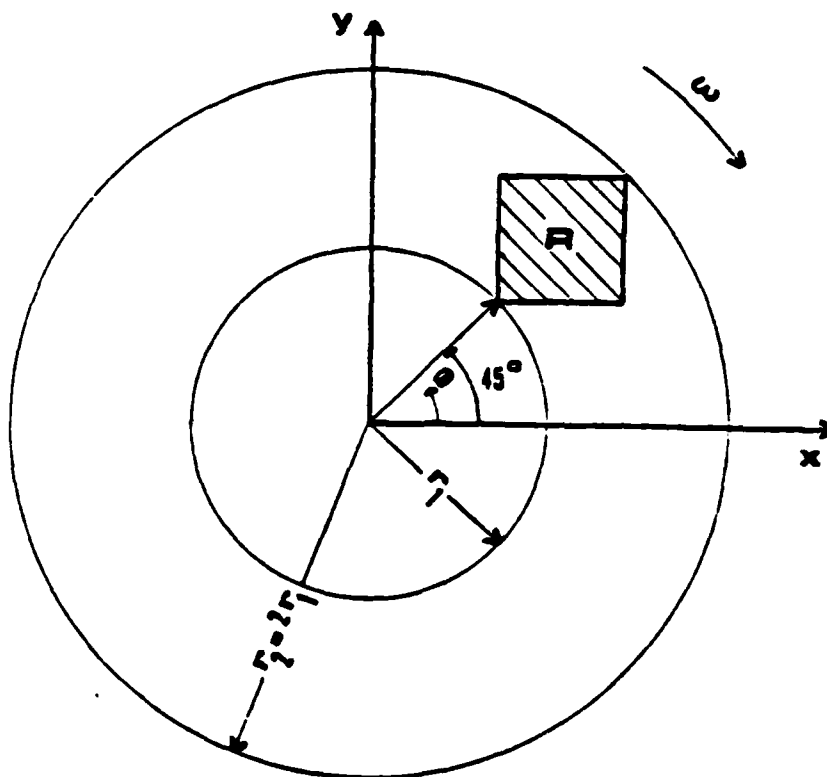


Fig. 3.1 Flow between rotating cylinders

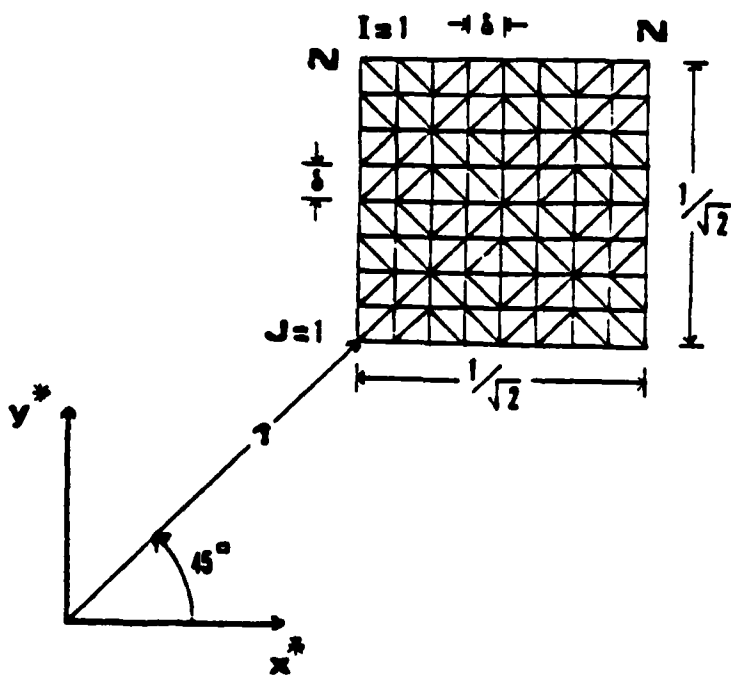


Fig. 3.2 Discretization of the calculation domain

Results

(i) Table 3-1(A) shows the variation of percentage error in u^* at the mid point of the computational domain with Reynolds number and grid size. The percentage error is defined as:

$$\text{percentage error in } u^* = 100 \left| \frac{u^*_{\text{exact}} - u^*_{\text{computed}}}{u^*_{\text{exact}}} \right| \quad (3.15)$$

where u^*_{exact} is the exact value of u^* given by Eq. (3.12) and u^*_{computed} is the numerically computed value.

As can be seen in Table 3-1(A), the percentage error increases with Reynolds number at any given grid size. For any given Reynolds number, the error decreases continuously as the grid is refined. Table 3-1(B) shows the results of unequal order method of Baliga and Patankar [2] for a 21 x 21 grid. Comparison of these with the present results for a 21 x 21 grid (Table 3-1(A)) shows that the proposed method gives lower error or better results.

(ii) Let $\bar{\epsilon}$ be the average of the percentage error defined in Eq. (3.15).

Further, let

$$\bar{\epsilon} = \alpha \delta^p \quad (3.16)$$

where α is a constant and p is the so-called 'order of convergence'. If $\bar{\epsilon}_1$ and $\bar{\epsilon}_2$ are the values of $\bar{\epsilon}$ for grid size δ_1 and δ_2 respectively, p can be determined from

$$p = \frac{\ln(\bar{\epsilon}_1) - \ln(\bar{\epsilon}_2)}{\ln(\delta_1) - \ln(\delta_2)} \quad (3.17)$$

Table 3-2(A) shows the variation of $\bar{\epsilon}$ with grid size and Reynolds number for the equal order method. Also included in this table are the values of order of convergence p obtained using the results of 17 x 17 and 21 x 21 grid. As can be seen, the percentage error over the domain, $\bar{\epsilon}$ increases with Reynolds number for any fixed grid size. Also, at any fixed Reynolds number $\bar{\epsilon}$ decreases with increasing grid size confirming that the computed solution converges to the exact solution as the grid is refined. From the tabulated values of p , it may be inferred that the order

TABLE 3-1(A)

Percentage error in u^* at the center of domain - equal order method

Grid	Re	1	10	100	1000
9 × 9		.0213	.149	.158	.837
13 × 13		.0107	.067	.268	.342
17 × 17		.00618	.0378	.238	.206
21 × 21		.00404	.0241	.193	.149

TABLE 3-1(B)

Percentage error in u^* at the center of domain - unequal order method

Grid	Re	1	10	100	1000
21 × 21		.02	.034	.264	.287

TABLE 3-2(A)

Average percentage error in u^* over the domain - equal order method

Re Grid; 8	1	10	100	1000
$9 \times 9; .125/\sqrt{2}$.0609	.0952	.337	.637
$13 \times 13; .0833/\sqrt{2}$.0251	.0442	.222	.345
$17 \times 17; .0625/\sqrt{2}$.0135	.025	.157	.226
$21 \times 21; .05/\sqrt{2}$.00846	.0162	.114	.166
Order of convergence p, using results of 17×17 21×21 grids	2.094	1.944	1.434	1.383

TABLE 3-2(B)

Average percentage error in u^* over the domain - unequal order method

Re Grid; 8	1	10	100	1000
$17 \times 17; .0625/\sqrt{2}$.050	.093	.545	.803
$21 \times 21; .05/\sqrt{2}$.034	.060	.407	.594
Order of convergence p	1.728	1.964	1.308	1.351

of convergence of the method is between 1 and 2.

Table 3-2(B) shows the corresponding results for the unequal order method of Baliga and Patankar [2].

(iii) Fig. 3.3(a) shows a comparison between the exact and computed solution for pressure distribution along the main diagonal of the computational domain. The computed results shown are for the finest, i.e., 21×21 grid. As is evident, the computed results are in excellent agreement with the exact solution for all values of Reynolds number.

Figure 3.3(b) shows the results obtained by using relatively coarse grids for a fixed Reynolds number of 1. It can be seen that the results are fairly good even at rather sparse grids. The error in the computed pressure distribution is higher at points close to the boundary of the domain compared to the errors at points which are in the core of the domain.

3.2 The driven cavity problem

The problem of flow in a square cavity with one moving wall is sketched in Fig. 3.4. As shown in this figure, three sides of the square cavity are at rest while the fourth, the top wall, moves tangentially with a velocity u_w . Burgraff [4] solved this problem using a very fine (52×52) grid. Burgraff's results are taken as a standard of comparison for the results obtained using the proposed equal order method.

Computational details

The computational domain is shown in Fig. 3.5. The domain discretization is also shown in this figure for a 13×13 grid. The grid was kept finer near the walls than in the core so that, at higher Reynolds numbers, the thin boundary layers close to the walls could be resolved. The position of the first two grid lines parallel to each wall was always kept fixed, being at a distance of .05 and .1 from the wall. Grid refinement only changed the spacing δ between the interior grid lines.

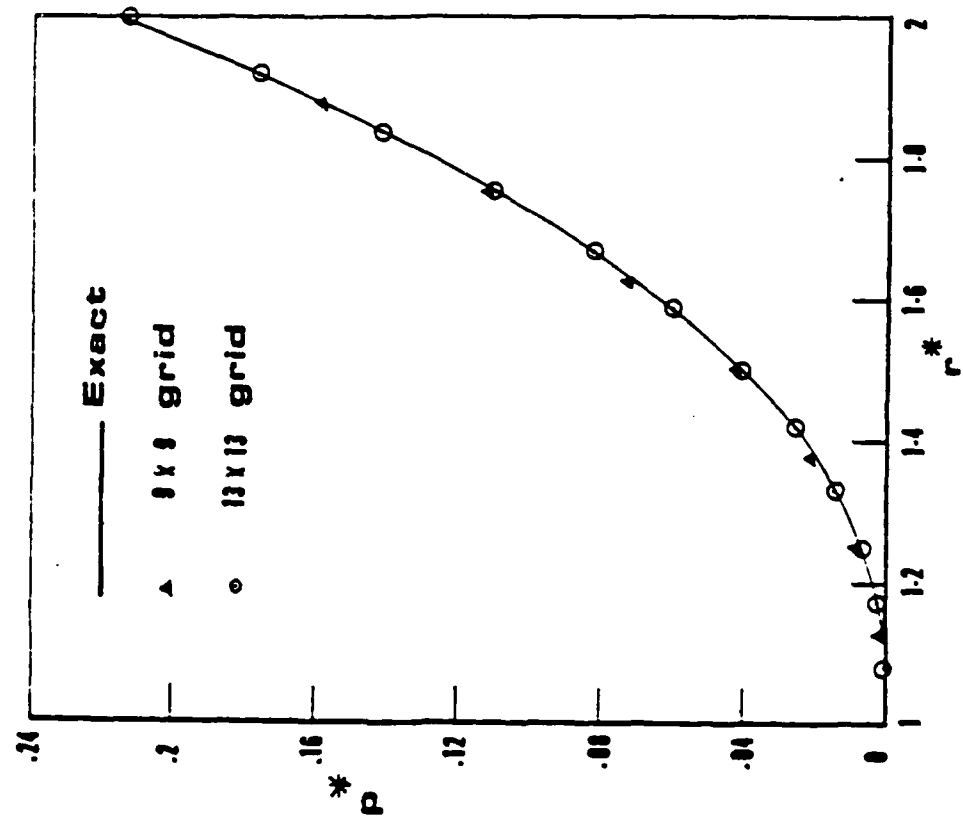


Fig. 3.3(b) Pressure distribution for coarser grids

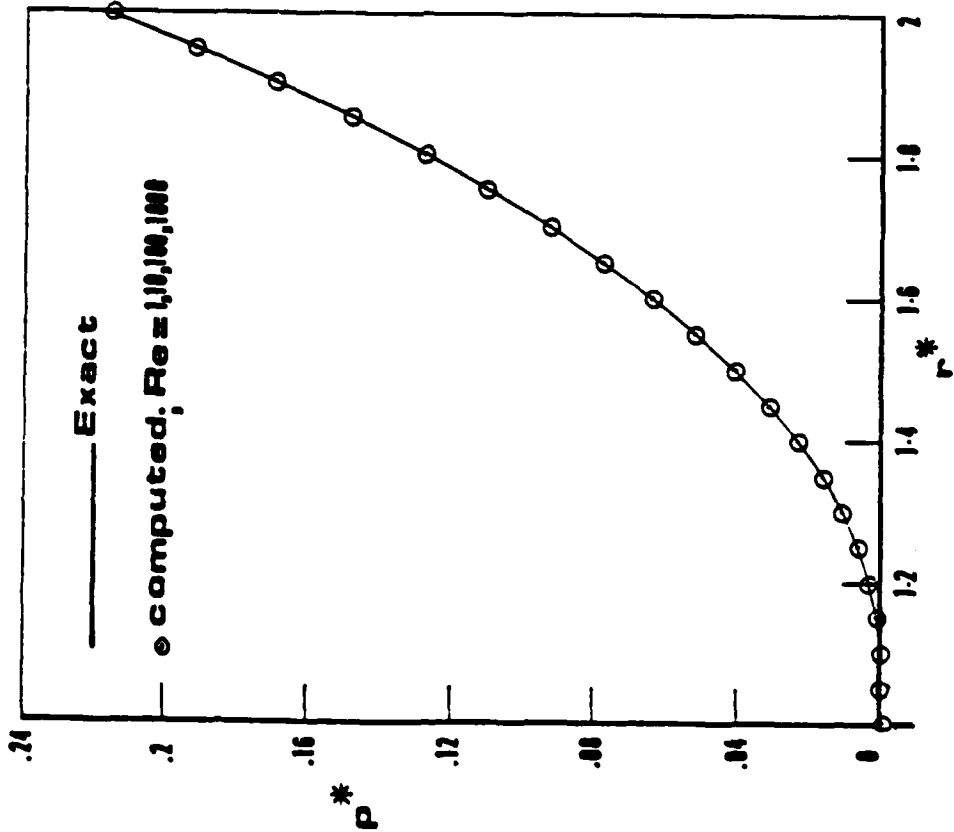


Fig. 3.3(a) Pressure distribution along the main diagonal for the 21x21 grid

Consequently, for a $N \times N$ grid,

$$\delta = \frac{1 - (.1) - (.1)}{(N-5)} = \frac{.8}{(N-5)} \quad (3.18)$$

Results

(i) Figure 3.6(a) shows results for the u velocity along the vertical center-line ($x = L/2$). The results of the equal order method are for a 21×21 ($N=21$) grid. At Reynolds numbers of 1 and 100, the computed results show very good agreement with the results of Burgraff; in particular, the difference between the two cannot be resolved on the graphical scale of Fig. 3.6(a). At a high Reynolds number of 400, the computed results are in fair agreement with the results of Burgraff except close to the region where the gradient of velocity, i.e. $\partial u / \partial y$, changes sign. It is possible that the 21×21 grid used for the equal order method is not enough to resolve the thin boundary layers close to the walls occurring for $Re = 400$.

Figure 3.6(b) shows how the solution evolves with grid refinement by the equal order method. The three grid sizes shown correspond to $N = 9, 13$ and 21 with corresponding δ (see Fig. 3.5) of $.2, .1$ and $.05$.

(ii) For two-dimensional incompressible flow, the stream function ψ is defined such that:

$$u = \frac{\partial \psi}{\partial y} \quad (3.19)$$

$$v = - \frac{\partial \psi}{\partial x} \quad (3.20)$$

from which it follows

$$\frac{\partial^2 \psi}{\partial x^2} + \frac{\partial^2 \psi}{\partial y^2} = \frac{\partial u}{\partial y} - \frac{\partial v}{\partial x} \quad (3.21)$$

After the velocity field had been computed, the Poisson equation (3.21) was solved numerically to get the stream function at all grid points.

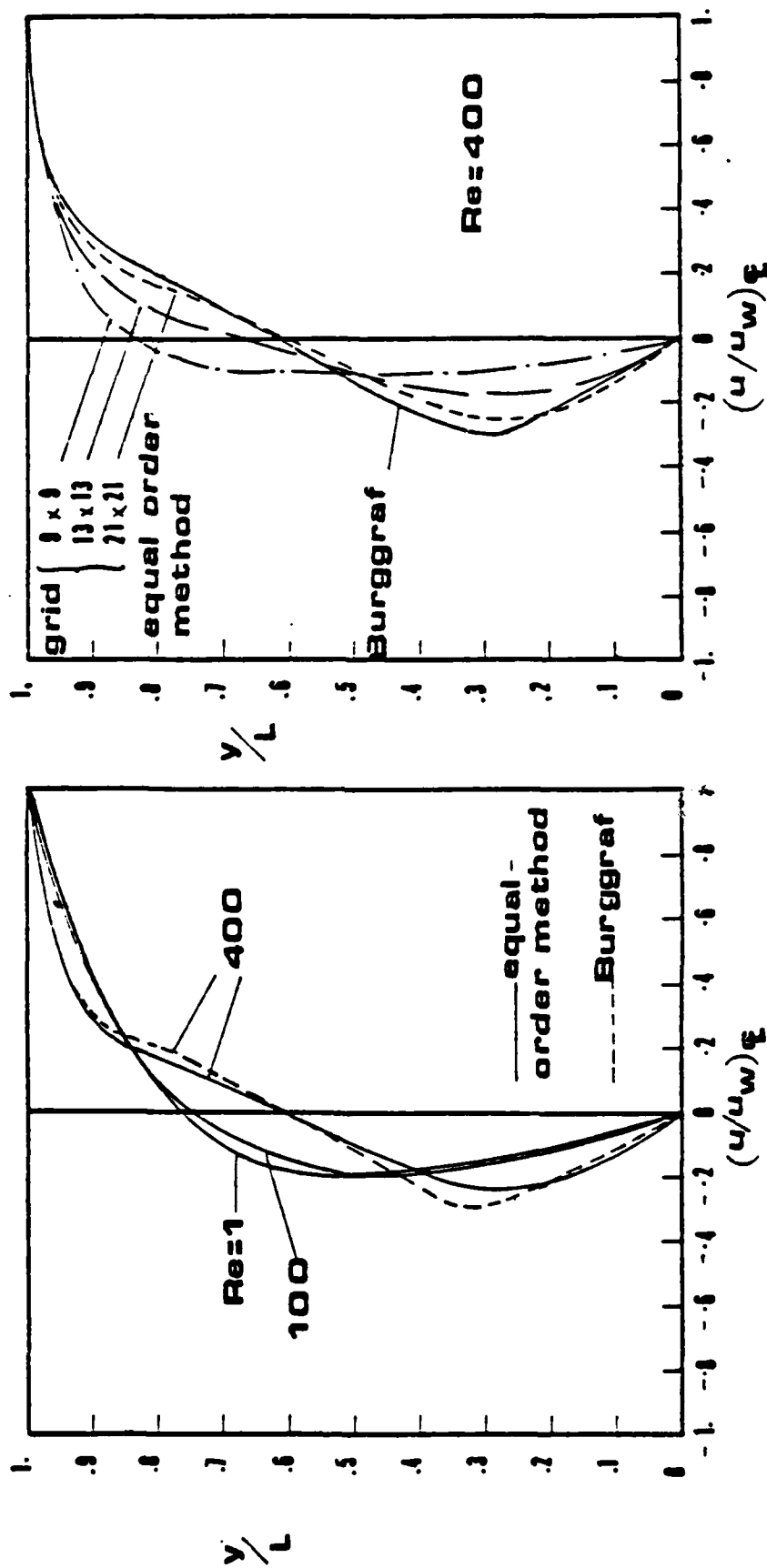


Fig. 3.6(a) Velocity profile on the vertical centerline for various Reynolds numbers

Fig. 3.6(b) Velocity profile for various grids

The streamline plots are shown in Figs. 3.7 - 3.9 for Reynolds number of 1, 100 and 400 respectively. The results computed by the proposed equal order method show a good agreement with the results of Burgraff. The separated flows at the bottom corners are correctly picked up at even coarse grids.

3.3 Natural convection in a square cavity

The problem of natural convection in a square cavity, shown schematically in Fig. 3.10, is used as another test problem. The hot and cold vertical walls are both isothermal at temperature T_H and T_C respectively. The top and bottom horizontal walls are adiabatic. The flow is assumed to be incompressible except for the calculation of driving buoyancy forces. Also, all properties of the fluid are assumed constant.

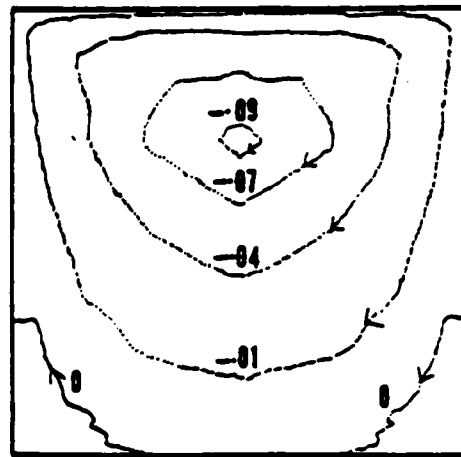
Since the problem does not have an exact analytic solution, the results computed by the proposed equal order method will be compared to those obtained by a finite difference technique on a very fine (32 x 32) grid. Because of the fine grid used, the results of the finite-difference method are regarded as "exact". The domain was discretized into a uniform $N \times N$ grid as shown in Fig. 3.11.

Results

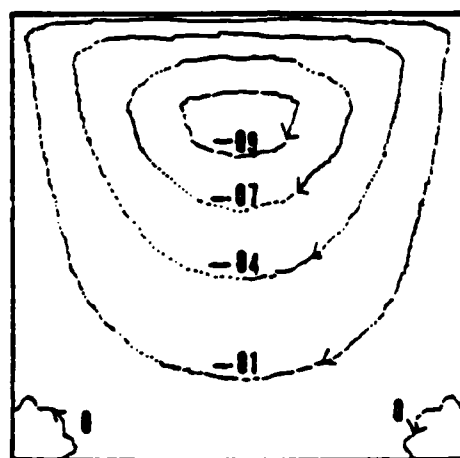
The problem is governed by two dimensionless parameters, namely, the Grashof number and the Prandtl number. In the presented computations, the value of Prandtl number was kept fixed at 1, while the Grashof number was assigned values 10^3 , 10^4 and 10^5 .

(i) Figures 3.12-3.14 show the variation of vertical velocity and temperature along the horizontal mid plane ($y/L = .5$) for Grashof numbers of 10^3 , 10^4 and 10^5 . Even though the results of the proposed method have been obtained on a coarser grid, their accuracy is as good as that given by the fine-grid finite-difference solution.

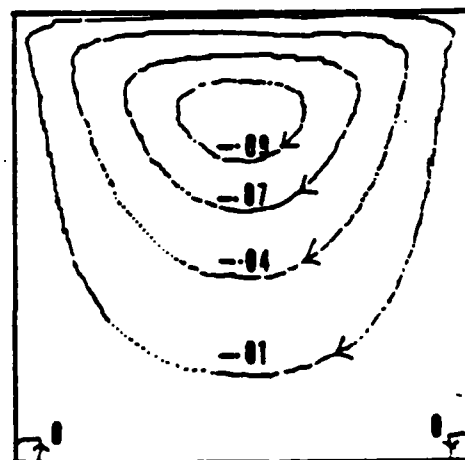
(ii) The average Nusselt number on the hot wall is defined as



9x9 Grid

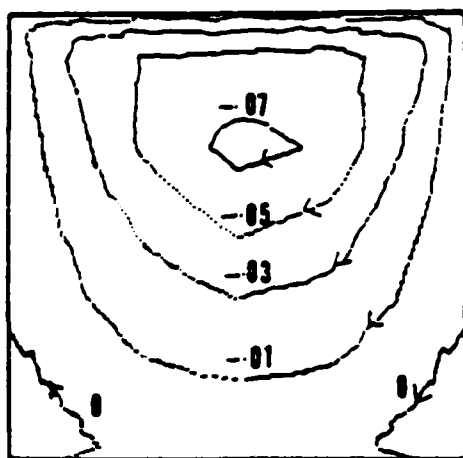


13x13 Grid

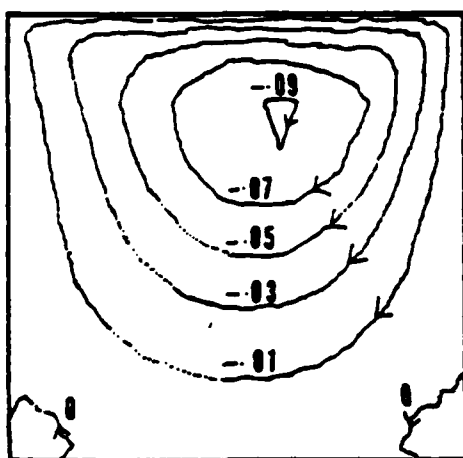


21x21 Grid

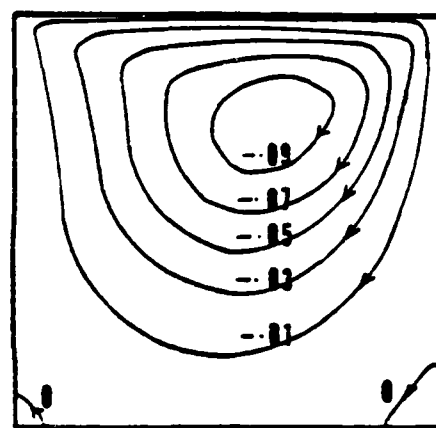
Fig. 3.7 Streamline patterns for $Re = 1$



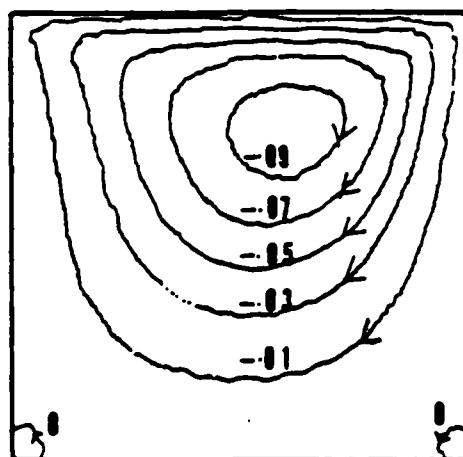
1x1 Grid



13x13 Grid

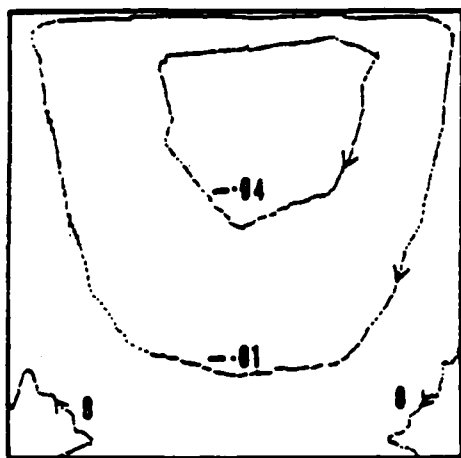


Burgraff

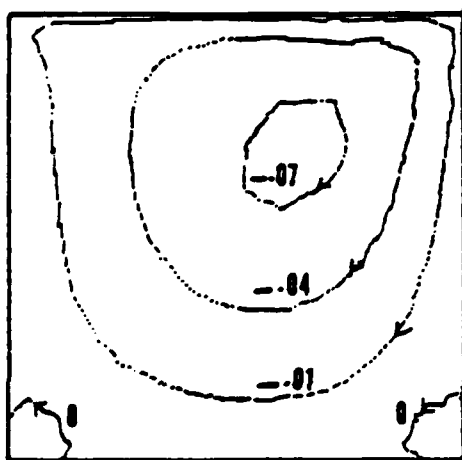


21x21 Grid

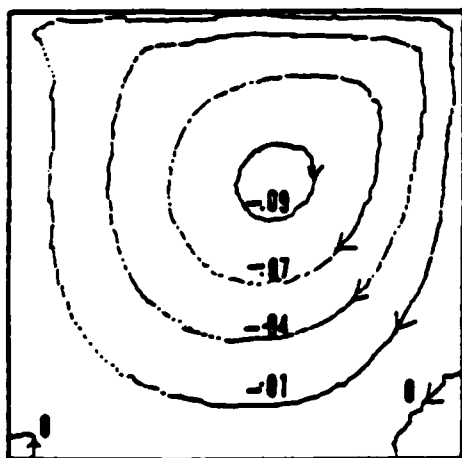
Fig. 3.8 Streamline patterns for $Re = 100$



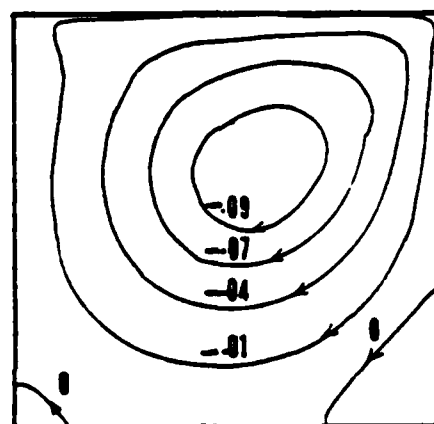
9x9 Grid



13x13 Grid



21x21 Grid



Burgreiff

Fig. 3.9 Streamline patterns for $Re = 400$

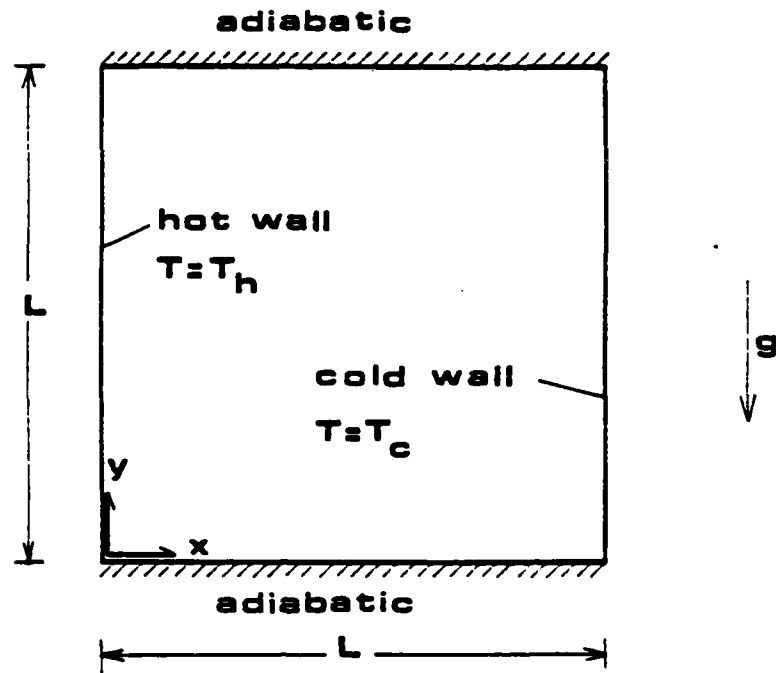


Fig. 3.10 Natural convection in a cavity

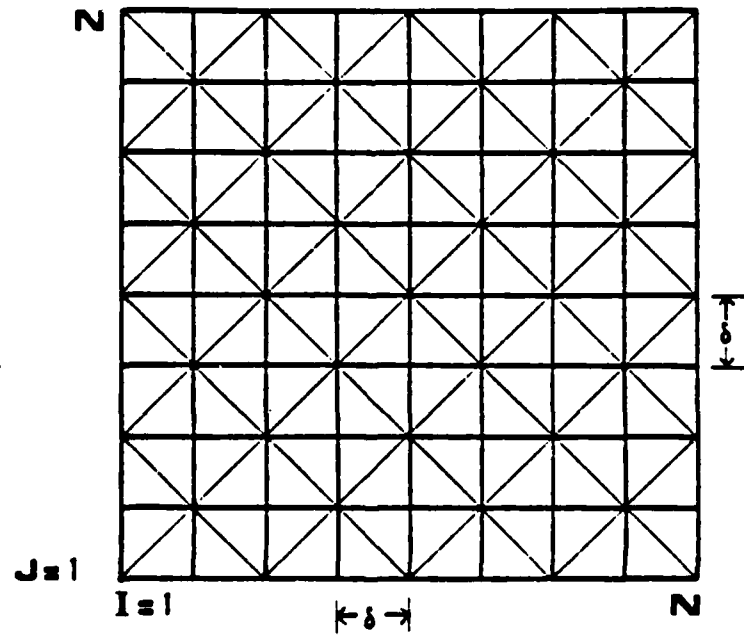


Fig. 3.11 Domain discretization

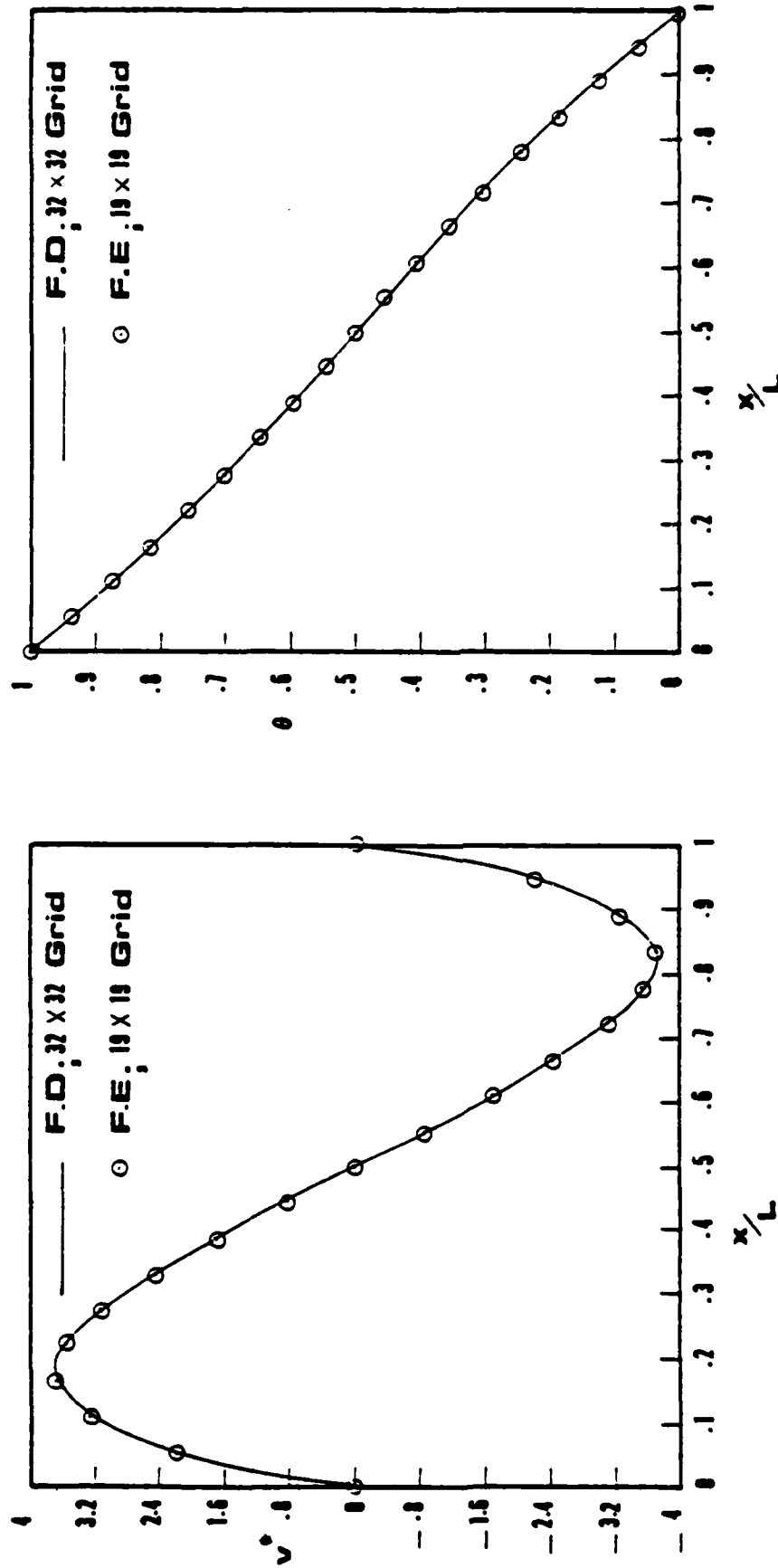


Fig. 3.12 Velocity and temperature distribution on the horizontal midplane, $Gr = 10^3$

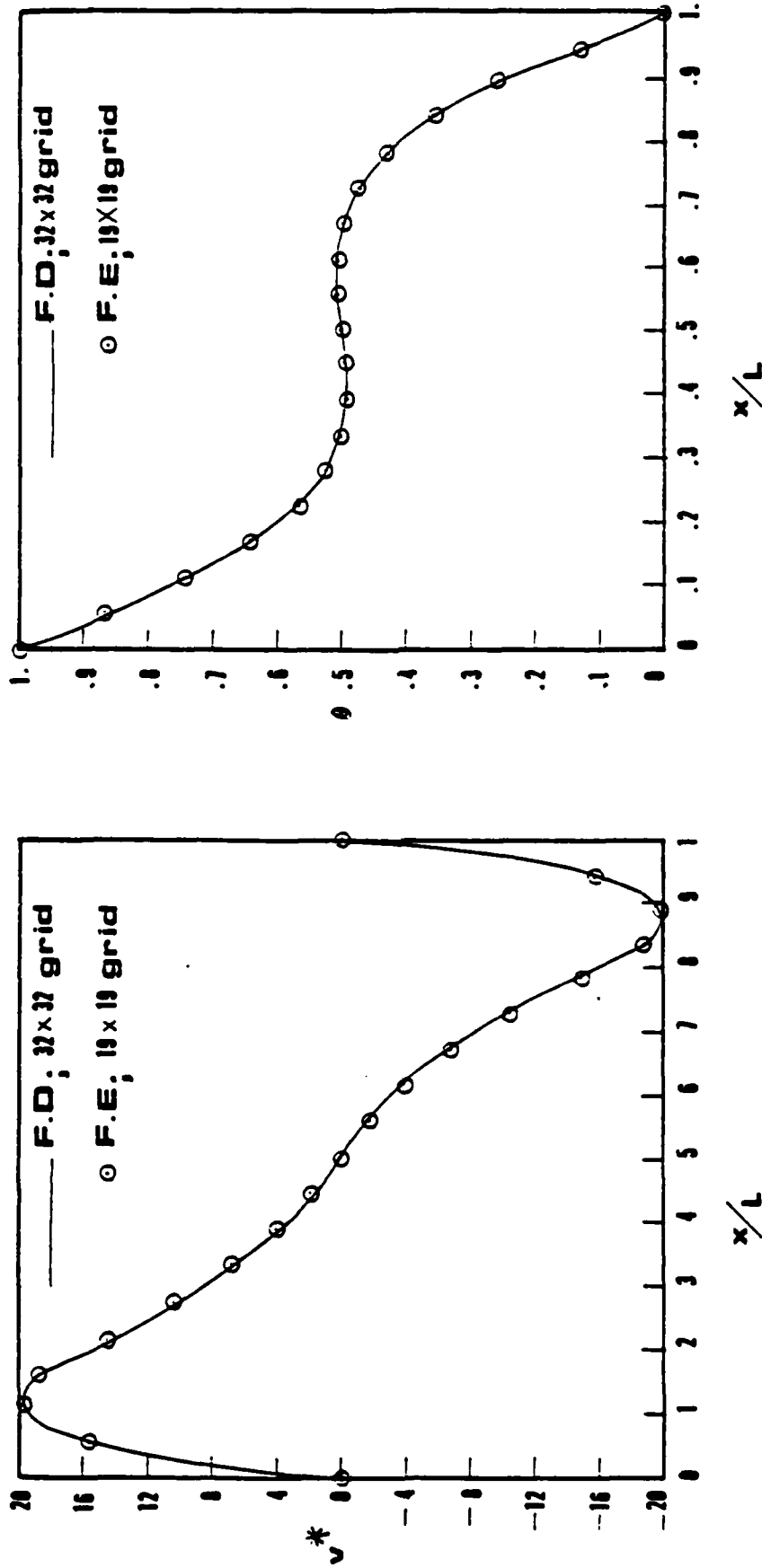


Fig. 3.13 Velocity and temperature distribution on the horizontal midplane, $Gr = 10^4$

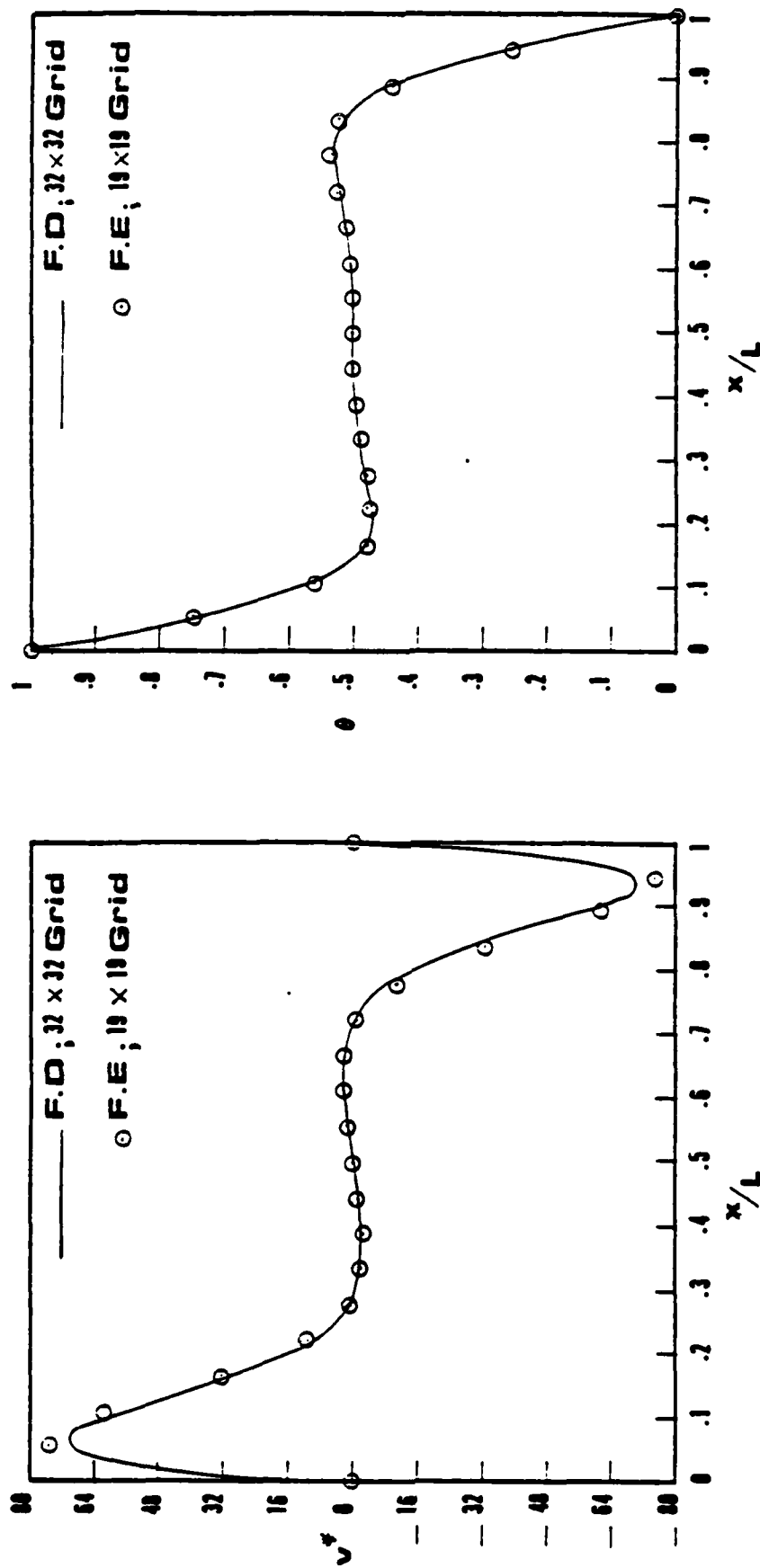


Fig. 3.14 Velocity and temperature distribution on the horizontal midplane, $Gr = 10^5$

$$Nu_{av} = \frac{h_{av} L}{k} \quad (3.22)$$

where, h_{av} is the average heat transfer coefficient defined from

$$h_{av} = \frac{q_{av}}{(T_H - T_C)} \quad (3.23)$$

q_{av} , the average heat flux being given by,

$$q_{av} = \frac{1}{L} \int_0^L q(y) dy \quad (3.24)$$

Table 3-3 shows the results for the average Nusselt number on the hot wall computed using the equal order method. The results have been cross tabulated against the grid size and Grashof number. For extrapolating the computed results to those corresponding to $\delta = 0$ (infinitely fine grid), a Richardson extrapolation has been applied. Thus

$$Nu_{av}(\delta) = Nu_{av}(0) + \alpha \delta^P \quad (3.25)$$

Table 3-3

Average Nusselt number in the duct, convergence study

Grid	δ	Nu_{av} for $Gr =$		
		10^3	10^4	10^5
11 x 11	.1	1.1084	2.2112	4.2611
15 x 15	.07143	1.1125	2.2302	4.4069
19 x 19	.05556	1.1146	2.2408	4.4719
Extrapolated value as $\delta \rightarrow 0$		1.1202	2.2793	4.5909
Value obtained by F D method; 32 x 32 Grid		1.1203	2.2825	4.7755

where α and p are some constants, and $Nu_{av}(0)$ is the value of Nu_{av} for $\delta = 0$. If Nu_{av} is computed for three values of δ , Equation (3.25) can be inverted to obtain $Nu_{av}(0)$, α and p . Table 3-3 includes the value of $Nu_{av}(0)$.

It is clear from Table 3-3 that the computed values of average Nusselt number are in very good agreement with those obtained by the fine-grid finite-difference method.

4. Method for three-dimensional duct flows

Three-dimensional duct flows can often be treated as fully parabolic, i.e. they can be solved by a marching procedure that begins at an upstream end and visits successive cross sections towards the downstream end. The computational problem at each cross section is essentially two-dimensional and the procedure described in Section 2 can be employed. The complete procedure for the three-dimensional duct flow is presented in this section.

4.1 Governing differential equation

For the coordinate system shown in Fig. 4.1, the counterpart of Eq. (2.1) for a three-dimensional parabolic flow can be written as

$$\begin{aligned} \frac{\partial}{\partial x} (\rho u \phi) + \frac{\partial}{\partial y} (\rho v \phi) + \frac{\partial}{\partial z} (\rho w \phi) \\ = \frac{\partial}{\partial x} \left(\Gamma \frac{\partial \phi}{\partial x} \right) + \frac{\partial}{\partial y} \left(\Gamma \frac{\partial \phi}{\partial y} \right) + S \end{aligned} \quad (4.1)$$

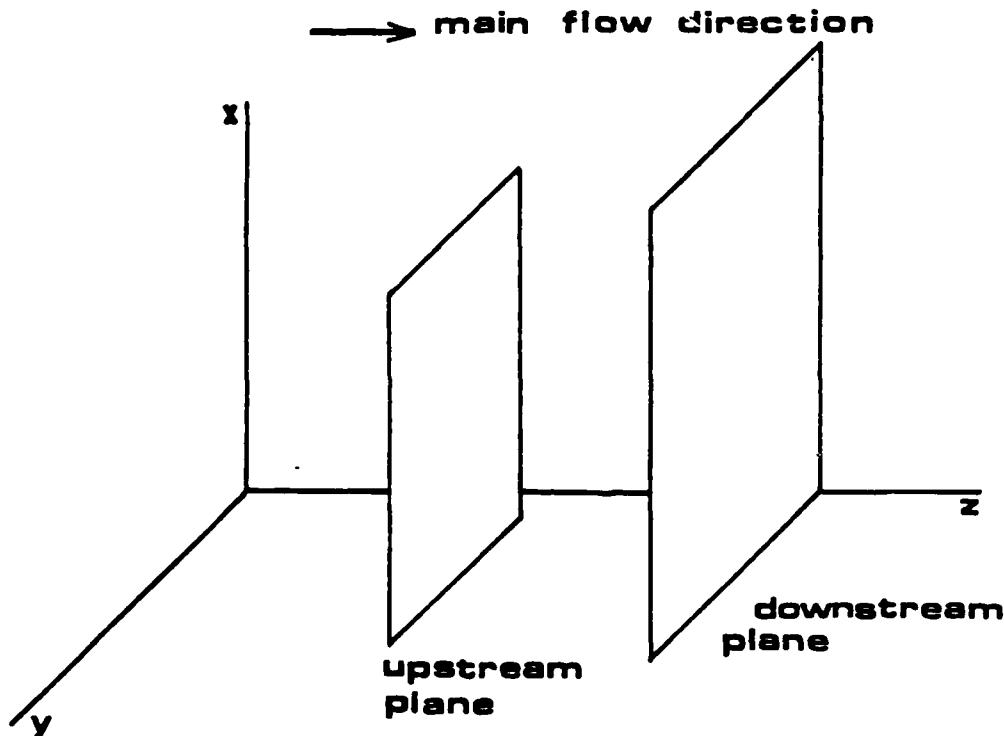


Fig. 4.1 Coordinate system

where the diffusion term in the main-stream direction z has been omitted in conformity with the boundary-layer (or parabolic-flow) assumption. Once again, the general dependent variable ϕ can stand for enthalpy, concentration, turbulence parameters, and the velocity components, u , v , and w . When ϕ equals u or v , the source terms S would contain the pressure gradient $-\partial p/\partial x$ or $-\partial p/\partial y$; these will be treated by the procedure described in Section 2. When ϕ stands for the main-stream velocity w , the source term would include $-\partial p/\partial z$. However, this will be replaced by $-d\bar{p}/dz$, where \bar{p} represents a cross-sectional mean pressure. To regard the velocity w to be "driven" by a mean pressure \bar{p} and not affected by the local variation of pressure p constitutes the basis of the fully parabolic treatment. If the velocity w is allowed to be influenced by the local pressure p , the resulting procedure is called partially parabolic. Construction of a partially parabolic procedure represents a later task in the current research project.

4.2 Domain discretization

The advantage of a marching or parabolic procedure is that, although the flow domain is three-dimensional, the entire duct need not be considered at once. At any given station, the computational problem is to obtain, from the known values of the variables on an upstream plane (see Fig. 4.1), the unknown values of the variables on the next downstream plane. Successive repetition of this basic operation is used to cover the total length of the duct. Restriction of the basic computational module to the region between two planes implies that computer storage is needed for the ϕ values only on the two planes and not throughout the entire duct.

The domain is discretized by forming triangular elements over the upstream and downstream planes. Corresponding typical elements are shown in Fig. 4.2. The shape of the two planes need not be rectangular; any arbitrary shape of the duct cross section can be adequately represented by triangular elements. Further, the

shape and size of the downstream plane need not match the upstream plane. Indeed, an ability to handle varying cross sections of arbitrary shape is one of the objectives of the proposed calculation method. Only when the cross section changes too rapidly from one station to the next, does the proposed fully parabolic procedure become inapplicable; then the problem should be solved by a partially parabolic or even a fully elliptic procedure.

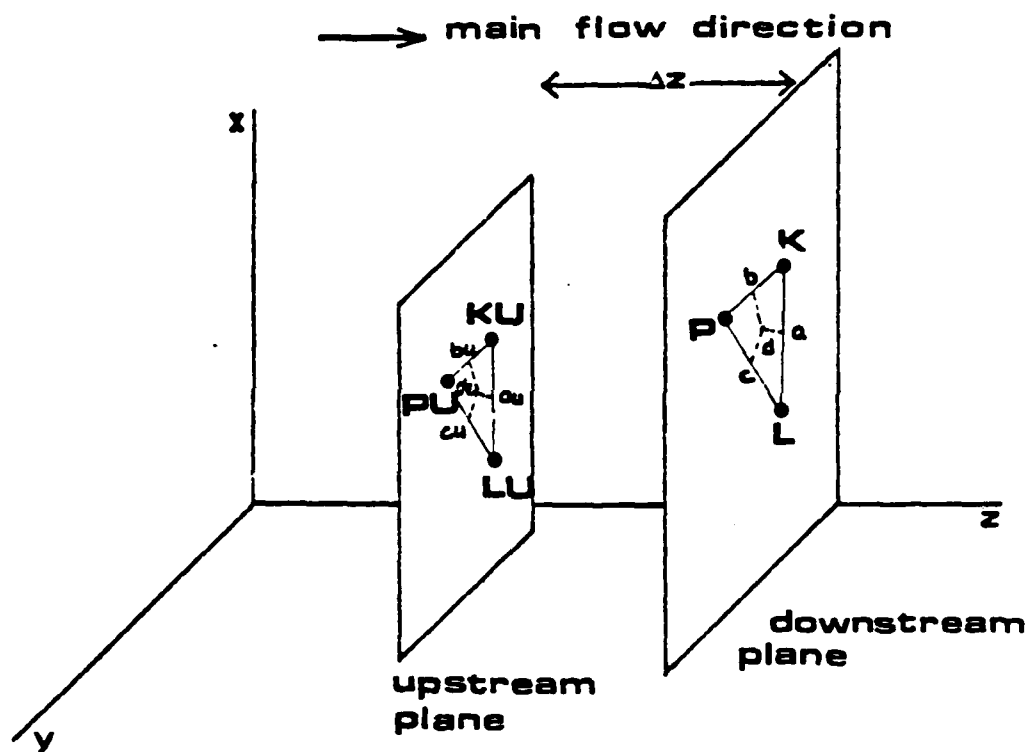


Fig. 4.2 Typical elements on the upstream and downstream planes

The triangulation on the two planes must, however, have the same number of triangles with a one-to-one correspondence between the elements. Thus, the triangulation of the downstream plane can be regarded as a stretched, compressed, or distorted version of the triangulation on the upstream plane. The element PKL shown in Fig. 4.2 corresponds to the element PU-KU-LU on the upstream plane: the size and orientation of these elements need not be the same. The dashed lines

show how each triangle is subdivided for the construction of the control volumes. The upstream and downstream faces of a typical control volume resemble the shaded region shown in Fig. 2.1. The lateral faces of the control volume are formed by quadrilaterals such as bu-b-d-du formed by the points shown in Fig. 4.2. The control volume has thus the shape of a prism with the shaded polygonal region in Fig. 2.1 as its base.

4.3 Discretization equation

The discretization form of Eq. (4.1) is obtained by integrating the equation over a typical control volume. For the convection and diffusion fluxes in the x and y directions (across the lateral faces of the control volume), the treatment described in Section 2.3 including the exponential shape function is employed. The z-direction convection across the upstream and downstream faces of the control volume is obtained by assuming that the values ϕ_{PU} and ϕ_P respectively prevail over these faces. Since it is possible that the lateral faces are not exactly parallel to the z axis, there may also be a z-direction convection across the lateral faces. This is calculated in terms of the ϕ value obtained at the control volume faces from the shape function (given by Eq. (2.2)).

In expressing the fluxes across the lateral faces, one is faced with the choice of using the (known) values of ϕ at the upstream plane, the (unknown) values of ϕ at the downstream plane, or some combination of these. Thus, the choice is between the explicit, fully implicit, or Crank-Nicolson formulations, or any other variants of these. As a result of the considerations expressed in [3], the fully implicit procedure is adapted here. Thus, the known ϕ values on the upstream plane are used only in the calculation of the convection through the upstream face of the control volume. All other influences in the discretization equation are expressed in terms of the unknown ϕ values on the downstream plane.

The final discretization equation can be written as

$$a_p \phi_p = \sum a_{nb} \phi_{nb} + a_{pu} \phi_{pu} + b \quad (4.2)$$

where a_{pu} is the mass flow rate through the upstream face of the control volume. With the values ϕ_{pu} known from the upstream plane, Eq. (4.2) has the same form as Eq. (2.3); therefore, the solution scheme outlined in Section 2.4 is applicable to Eq. (4.2) as well.

4.4 Calculation of the overall pressure gradient

In a duct flow, the pressure gradient $d\bar{p}/dz$ driving the z-direction velocity w is not known beforehand. It must adjust itself so that a given mass flow rate \dot{M} can be maintained in the duct despite the resistance offered by the duct walls. Thus, the satisfaction of the overall mass conservation is a constraint that permits the determination of $d\bar{p}/dz$.

The discretization equation for the mainstream velocity w can be written along the lines of Eq. (4.2). It is

$$a_p w_p = \sum a_{nb} w_{nb} + a_{pu} w_{pu} + b - (\Delta V) (d\bar{p}/dz) \quad (4.3)$$

where the pressure-gradient term is written separately; its multiplier ΔV is the volume of the control volume. The determination of $d\bar{p}/dz$ is based on the procedure suggested by Raithby and Schneider [5]. The main idea of the procedure is that, for a given set of coefficients, all the w values on the downstream plane are linearly dependent on $d\bar{p}/dz$. Thus

$$w_p = \alpha_p - \beta_p (d\bar{p}/dz) \quad (4.4)$$

where α_p and β_p are unknown constants associated with each node P . Equation (4.4) can be substituted into Eq. (4.3). Since the resulting relation must hold for any value of $d\bar{p}/dz$, two separate equations can be derived: one composed of terms that do not contain $d\bar{p}/dz$ and the other composed of the coefficients of $d\bar{p}/dz$. Thus,

$$a_p \alpha_p = \sum a_{nb} \alpha_{nb} + a_{PU} w_{PU} + b \quad (4.5)$$

and

$$a_p \beta_p = \sum a_{nb} \beta_{nb} + \Delta V \quad (4.6)$$

These equations have the same general form of Eq. (4.2) and can be solved in a similar fashion to obtain α_p and β_p for every node.

The total mass flow rate \dot{M} through the duct is given by

$$\dot{M} = \sum \rho_p A_p w_p \quad (4.7)$$

where ρ_p and A_p denote the density and area associated with the downstream face of the control volume and the summation is taken over the entire downstream plane.

Combination of Eqs. (4.4) and (4.7) gives

$$d\bar{p}/dz = (\dot{M} - \sum \rho_p A_p \alpha_p) / (\sum \rho_p A_p \beta_p) \quad (4.8)$$

4.5 The overall solution procedure

The complete solution of a three-dimensional duct flow is obtained by repeating the solution for one forward step in the z direction. For the first forward step, the values of ϕ on the upstream or the inlet plane are given as a part of the problem specification. For subsequent forward steps, the ϕ values obtained on the downstream plane of the previous step become available as the upstream-plane values for the current step. With this general framework, it is now sufficient to describe the details of the calculation for one forward step. The various steps in the calculation sequence are outlined here.

- (1) Start with the initial guess for the ϕ values for the downstream plane. Usually, the known ϕ values on the upstream plane serve as satisfactory guesses.
- (2) Calculate the discretization coefficients for the three momentum equations.
- (3) Using these coefficients, solve Eqs. (4.5) and (4.6) to obtain the fields of α and β .
- (4) Determine $d\bar{p}/dz$ from Eq. (4.8) and hence obtain the values of w from Eq. (4.4).

(5) Now calculate \hat{u} , \hat{v} , d^u , and d^v from Eqs. (2.7), (2.8), and (2.11) appropriately written for the three-dimensional control volume.

(6) Hence solve the three-dimensional counterpart of Eq. (2.14) to obtain the pressure field.

(7) Considering this as p^* , solve the cross-stream momentum equations to get u^* and v^* .

(8) Now set up the pressure-correction equation (2.16) and solve it. Use the resulting p' values to correct \tilde{u}^* , \tilde{v}^* , u^* , and v^* .

(9) Solve Eq. (4.2) for other relevant variables such as temperature, concentration, turbulence parameters, etc.

(10) Return to step 2 and repeat until convergence.

(11) Treat the downstream ϕ values as the upstream values for the next forward step and return to step 1 to begin the calculation sequence for the next Δz .

5. Application of the method to some three-dimensional duct flows

In this section, results obtained by applying the proposed method to some three-dimensional ducts flows are presented. The results are divided into two sub-sections: In Section 5.1, ducts of uniform cross-sectional shape and area are considered; in Section 5.2, ducts of variable cross section are treated.

5.1 Flow through ducts of uniform cross section

Here, two duct geometries are considered. The first example involves developing flow in a square duct. The second example considers the flow over rod bundles. This problem demonstrates the capability of the proposed method to handle flow through ducts of complex (irregular) cross-sectional shapes.

5.1-1 Developing flow in a square duct

The flow situation considered is shown schematically in Fig. 5.1. A uniform flow enters a square duct at the entrance plane $z = 0$. As the flow moves along the duct, boundary layers on the duct walls grow continuously. After a certain distance, they merge into each other and the flow tends to attain a fully developed character. Such a fully developed flow is characterized by zero cross-stream velocities, i.e., $u = v = 0$, and an axial velocity w which is independent of the axial location z . Further, in fully developed flow, the axial pressure gradient $d\bar{p}/dz$ becomes independent of z and hence \bar{p} decreases linearly with z .

Computational details

Because of symmetry, only one fourth of the duct is used for computational purposes. Figure 5.2 shows the cross section of one fourth of the duct and its discretization into triangular elements. As can be seen, a uniform grid having $N \times N$ grid points is used. For a $N \times N$ grid, the spacing between adjacent grid points is given by δ where

$$\delta = \frac{0.5}{(N-1)} \quad (5.1)$$

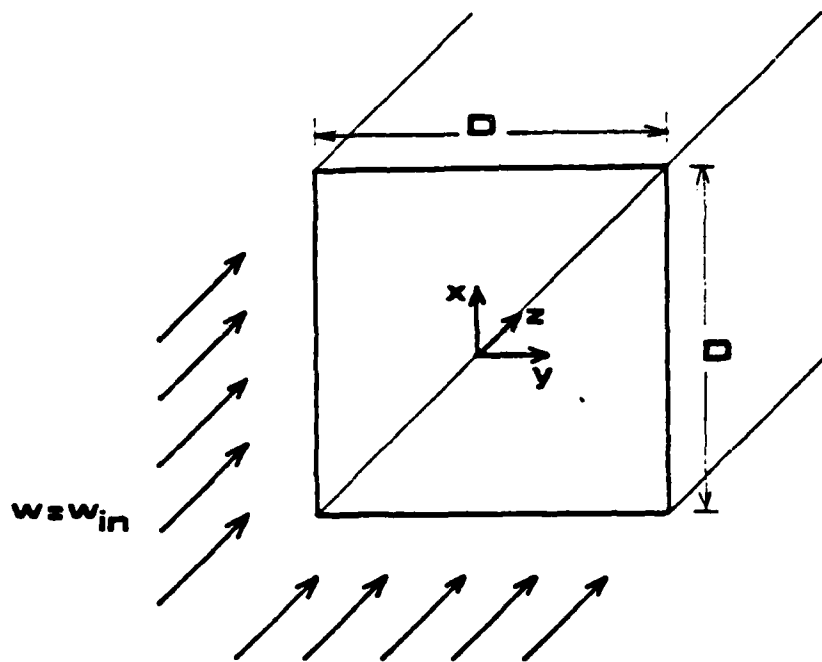


Fig. 5.1 Geometry of the square duct

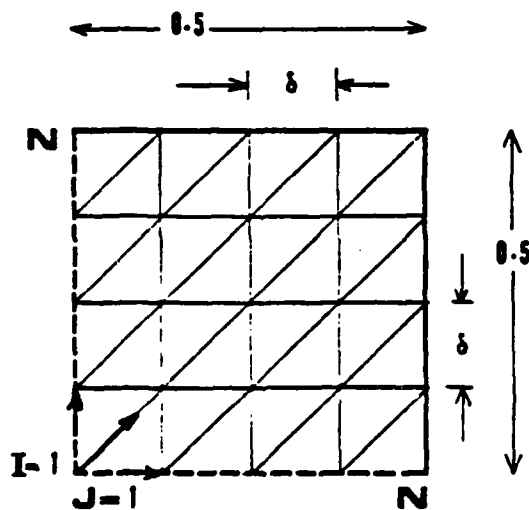


Fig. 5.2 Discretization of the domain

Results

(i) The dependence of the computed results on the grid parameters Δz and δ is shown by reference to fRe , where f is the friction factor defined as

$$f = \left(-\frac{dp}{dz}\right) \frac{D}{\frac{1}{2}\rho w^2} \quad (5.2)$$

and Re is the Reynolds number given by

$$Re = \frac{\rho w D}{\mu} \quad (5.3)$$

Figure 5.3 shows the computed variation of fRe with dimensionless axial distance. Results obtained by using different step sizes Δz and different number of grid points in the cross-stream plane are shown. The finest grid used for the results displayed in Fig. 5.3 corresponds to a dimensionless step size of .0005 and a 17 x 17 grid in the cross-stream plane. All the remaining results to be presented are based on this grid.

(ii) The variation of mean pressure \bar{p} with axial distance z is shown in Fig. 5.4(a). Also shown are the experimental results of Beavers, et al [6]. The agreement between the computed and experimental results is very good.

Figure 5.4(b) shows the variation of axial velocity at the centerline of the duct. The experimental results of Goldstein and Kreid [7] have also been plotted for comparison. Once again, the agreement between the computed and experimental results is very good.

5.1-2 Developing flow over rod bundles

The second test problem involves computation of developing flow over rod bundles which are arranged in a regular equilateral triangular array. The situation is shown schematically in Fig. 5.5. Such a flow configuration arises in nuclear reactors, compact heat exchangers and many other engineering applications.

Computational details

Because of symmetry, the calculation can be confined to the region shown in Fig. 5.6. The corresponding triangulation is also shown. A 17 x 17 grid was used.

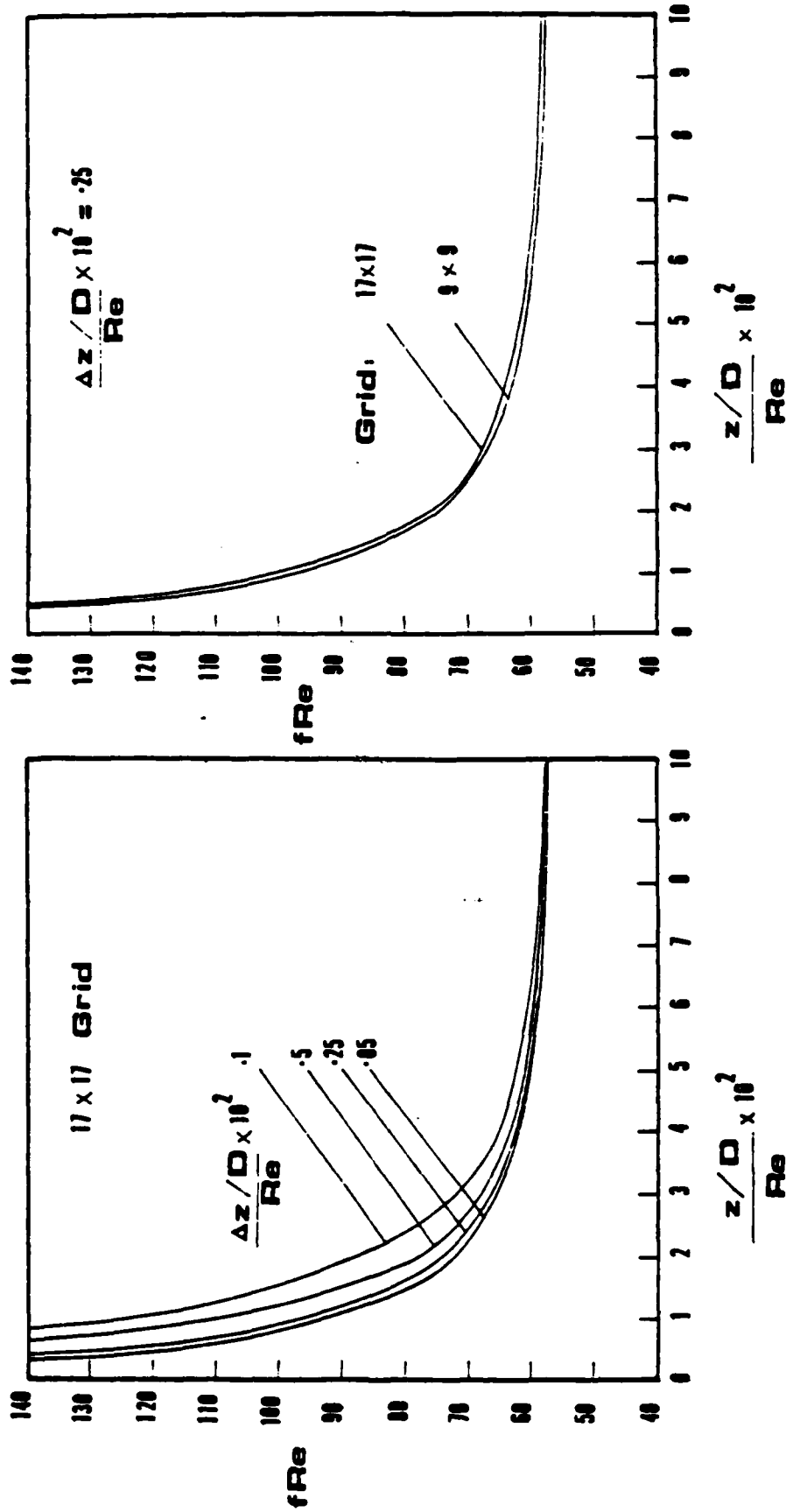


Fig. 5.3 Variation of fRe with the streamwise distance

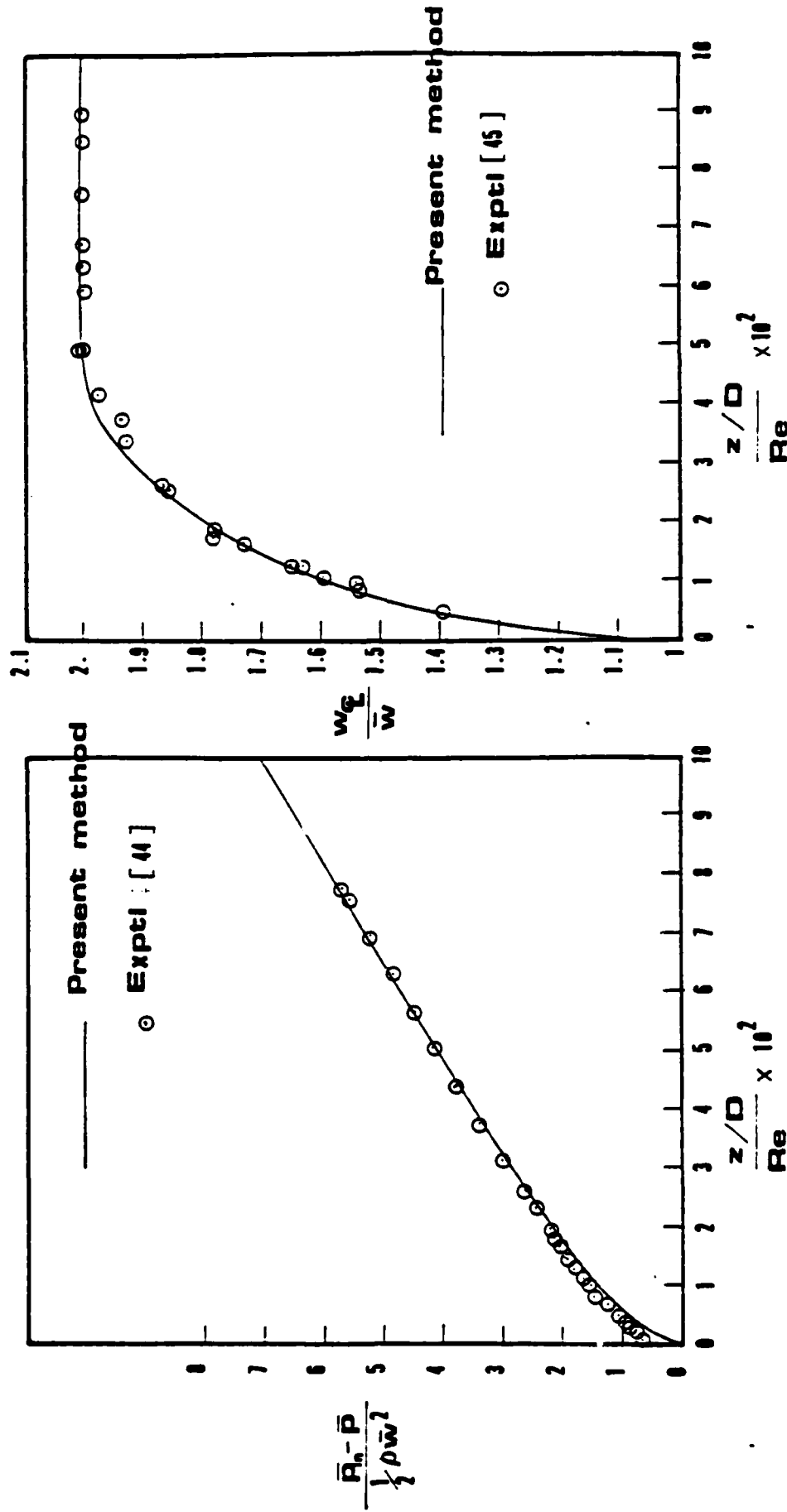


Fig. 5.4(a) Variation of pressure with axial distance

Fig. 5.4(b) Variation of the centerline velocity

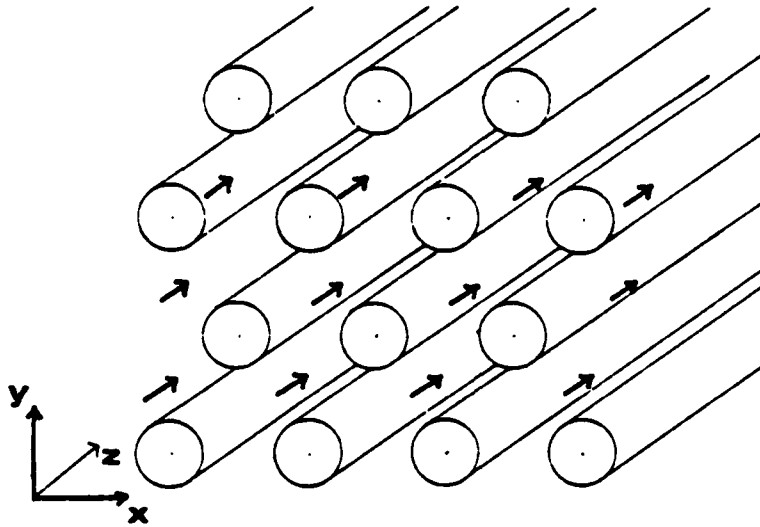


Fig. 5.5 Flow configuration

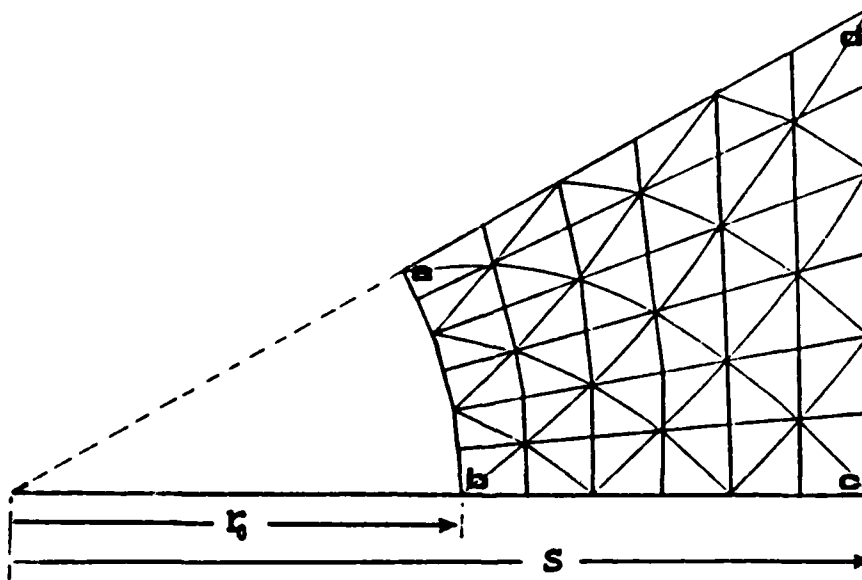


Fig. 5.6 Domain discretization

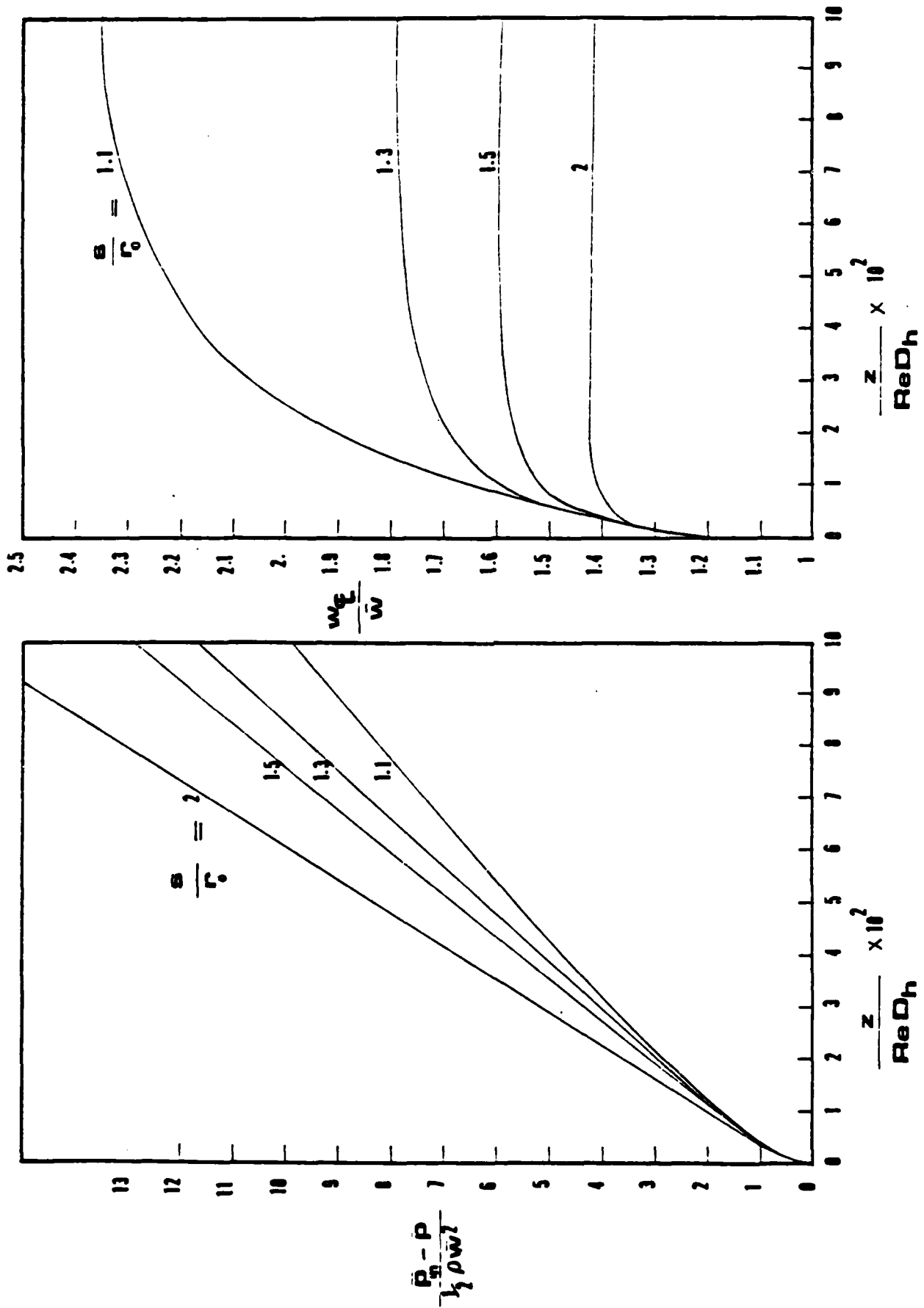


Fig. 5.7(a) Variation of pressure with streamwise distance

Fig. 5.7(a) Variation of the centerline velocity

Figure 5.7(a) shows the variation of pressure \bar{p} with axial distance for different values of the geometrical parameter s/r_0 . The development of centerline velocity is shown in Fig. 5.7(b). The fully developed values of the centerline w are in good agreement with those obtained by Sparrow and Loeffler [8].

5.2 Flow through ducts of varying cross-sectional shape and area

The most important feature of the proposed method is its capability to compute the flow through ducts of varying cross-sectional shape and area. Since no experimental or analytical results are available for such ducts, a procedure is devised here to "fabricate" exact solutions for developing flow in ducts of varying cross sections. These exact solutions are used to check the accuracy of the numerical solution.

5.2-1 Formulation of the exact solutions

The central idea of the method can be summarized as follows:

(i) Propose a velocity field \vec{u}_{exact} which satisfies the continuity equation and certain boundary conditions. Also propose a pressure field.

(ii) Compute the source terms in the momentum equations, S^u , S^v , and S^w , such that the velocity field \vec{u}_{exact} satisfies the momentum equations.

If the resulting expressions for the source terms are considered as given "body forces" in the problem specification, then \vec{u}_{exact} is indeed the exact solution of the flow equations (along with the assumed pressure field).

Case A: Square diffuser with parabolic velocity profile

For a square-sectioned diffuser, shown in Fig. 5.8, the half-side D linearly increases at a rate of $dD/dz = \alpha$. The exact solution for the velocity field is given by

$$w = \frac{9}{16} \frac{\dot{M}}{\rho} \frac{(D^2 - y^2)(D^2 - x^2)}{D^6} \quad (5.4)$$

$$u = \frac{9}{16} \frac{\dot{M}}{\rho} \frac{x}{D} \gamma \frac{(D^2 - y^2)(D^2 - x^2)}{D^6} \quad (5.5)$$

$$v = \frac{9}{16} \frac{\dot{M}}{\rho} \frac{\gamma\gamma}{D} \frac{(D^2 - \gamma^2)(D^2 - x^2)}{D^6} \quad (5.6)$$

$$\frac{\partial p}{\partial x} = 0 \quad (5.7)$$

$$\frac{\partial p}{\partial y} = 0 \quad (5.8)$$

$$- \frac{dp}{dz} = - \frac{9}{50} \frac{\dot{M}^2}{\rho} \frac{\gamma}{D^5} + \frac{3}{2} \frac{\dot{M}}{\rho} \frac{\mu}{D^4} \quad (5.9)$$

$$s^u = \frac{9}{8} \frac{\dot{M}}{\rho} \frac{\mu}{D^7} \gamma x [3(D^2 - \gamma^2) + (D^2 - x^2)] \\ - \frac{81}{128} \frac{\dot{M}^2}{\rho} \frac{\gamma x}{D^{14}} (D^2 - \gamma^2)^2 (D^2 - x^2)^2 \quad (5.10)$$

$$s^v = \frac{9}{8} \frac{\dot{M}}{\rho} \frac{\mu}{D^7} \gamma y [3(D^2 - x^2) + (D^2 - \gamma^2)] \\ - \frac{81}{128} \frac{\dot{M}^2}{\rho} \frac{\gamma y}{D^{14}} (D^2 - \gamma^2)^2 (D^2 - x^2)^2 \quad (5.11)$$

$$s^w = \frac{9}{8} \frac{\dot{M}}{\rho} \frac{\mu}{D^6} [(D^2 - x^2) + (D^2 - \gamma^2) - \frac{4}{3} D^2] \\ - \frac{81}{128} \frac{\dot{M}^2}{\rho} \frac{\gamma}{D^{13}} [(D^2 - x^2)^2 (D^2 - \gamma^2)^2 - \frac{64}{225} D^8] \quad (5.12)$$

where \dot{M} is the mass flow rate through the duct.

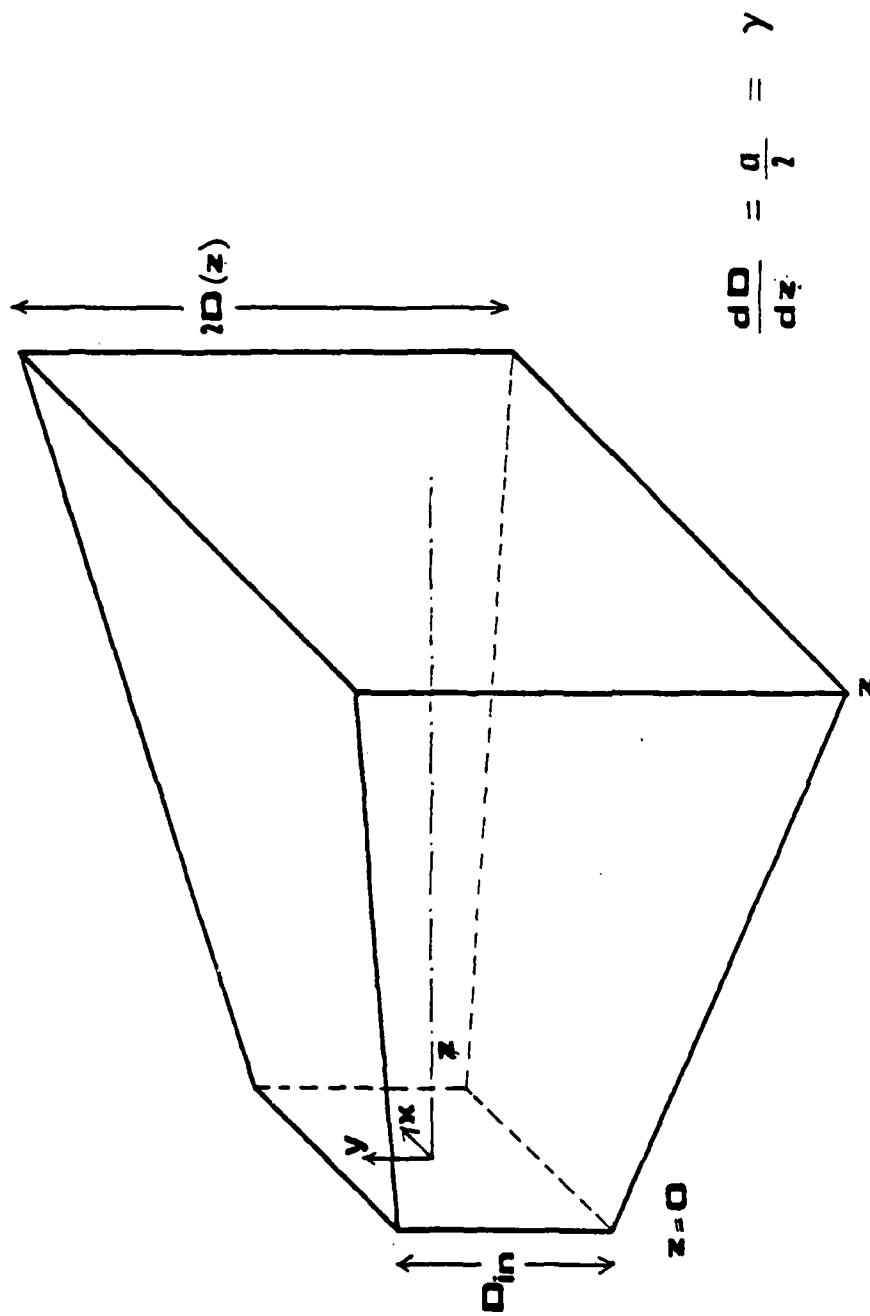


Fig. 5.8 Geometry of the square diffuser

Case B: Elliptic ducts

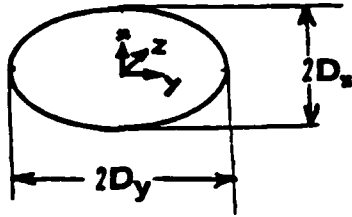


Fig. 5.9 Cross section of an elliptic duct

The cross section of an elliptic duct is shown in Fig. 5.9. The semi-major axis D_y and the semi-minor axis D_x are both functions of the axial coordinate z . Let the variation of D_x and D_y be given by:

$$D_x = D_0 + \gamma z \quad (5.13)$$

and

$$D_y D_x = \text{constant} = D_0^2 \quad (5.14)$$

where γ and D_0 are two arbitrary constants. Thus, at $z = 0$, the cross-section of the duct is a circle of radius D_0 . The exact solution for the velocity field can be expressed as

$$w = \frac{2}{\pi} \frac{\dot{M}}{\rho} \frac{1}{D_0^6} [(D_x^2 - x^2) + (D_y^2 - y^2)] \quad (5.15)$$

$$u = \frac{2}{\pi} \frac{\dot{M}}{\rho} \gamma \left(\frac{x}{D_x} \right) \frac{1}{D_0^6} [(D_x^2 - x^2) + (D_y^2 - y^2)] \quad (5.16)$$

$$v = \frac{2}{\pi} \frac{\dot{M}}{\rho} \beta \left(\frac{y}{D_0} \right) \frac{1}{D_0^6} [(D_x^2 - x^2) + (D_y^2 - y^2)] \quad (5.17)$$

$$\frac{\partial p}{\partial x} = 0 \quad (5.18)$$

$$\frac{\partial p}{\partial y} = 0 \quad (5.19)$$

$$- \frac{dp}{dz} = \frac{4}{\pi} \frac{\dot{M}}{\rho} \frac{\mu}{D_0^6} [D_x^2 + D_y^2] \quad (5.20)$$

provided that the source terms in the momentum equations are given by

$$s^u = \frac{4}{\pi} \frac{\dot{M}}{\rho} \frac{\mu}{D_0^6} \gamma \left(\frac{x}{D_0} \right) [3D_y^2 + D_x^2] \quad (5.21)$$

$$\begin{aligned} s^v = & - \frac{8}{\pi^2} \frac{\dot{M}^2}{\rho} \frac{\gamma \beta}{D_0^{10}} \gamma [(D_x^2 - x^2) + (D_y^2 - y^2)] \\ & + \frac{4}{\pi} \frac{\dot{M}}{\rho} \frac{\mu}{D_0^6} \beta \left(\frac{y}{D_0} \right) [3D_x^2 + D_y^2] \end{aligned} \quad (5.22)$$

and

$$S^w = 0 \quad (5.23)$$

Here, the coefficient β is defined as

$$\beta = \frac{dD_y}{dz} \quad (5.24)$$

In the use of the calculation procedure for these test problems, computations were performed both with and without the momentum source terms. The results of the former can be compared with the exact solutions, while the latter computation shows how the flow will behave in reality without the artificial "body forces".

5.2-2 Flow through a square diffuser

With reference to Fig. 5.8, the geometry of the square diffuser is defined in terms of:

$$2D = D_{in} + \alpha z \quad (5.25)$$

Thus,

$$D = \frac{D_{in}}{2} + \frac{\alpha}{2} z \quad (5.26)$$

or

$$D = D_0 + \gamma z \quad (5.27)$$

where

$$D_0 = D_{in}/2 \quad (5.28)$$

$$\gamma = \alpha/2 \quad (5.29)$$

The computations were performed by using a 17 x 17 grid similar in pattern to the one in Fig. 5.2.

Figure 5.10 shows the variation of axial pressure gradient $d\bar{P}/dZ$ with Z , where the dimensionless distance Z is defined by

$$Z = z / (Re_{in} D_{in}) \quad (5.30)$$

Figure 5.10(a) shows the results with the source terms, while Fig. 5.10(b) displays the implications of the usual momentum equations. The dashed lines in

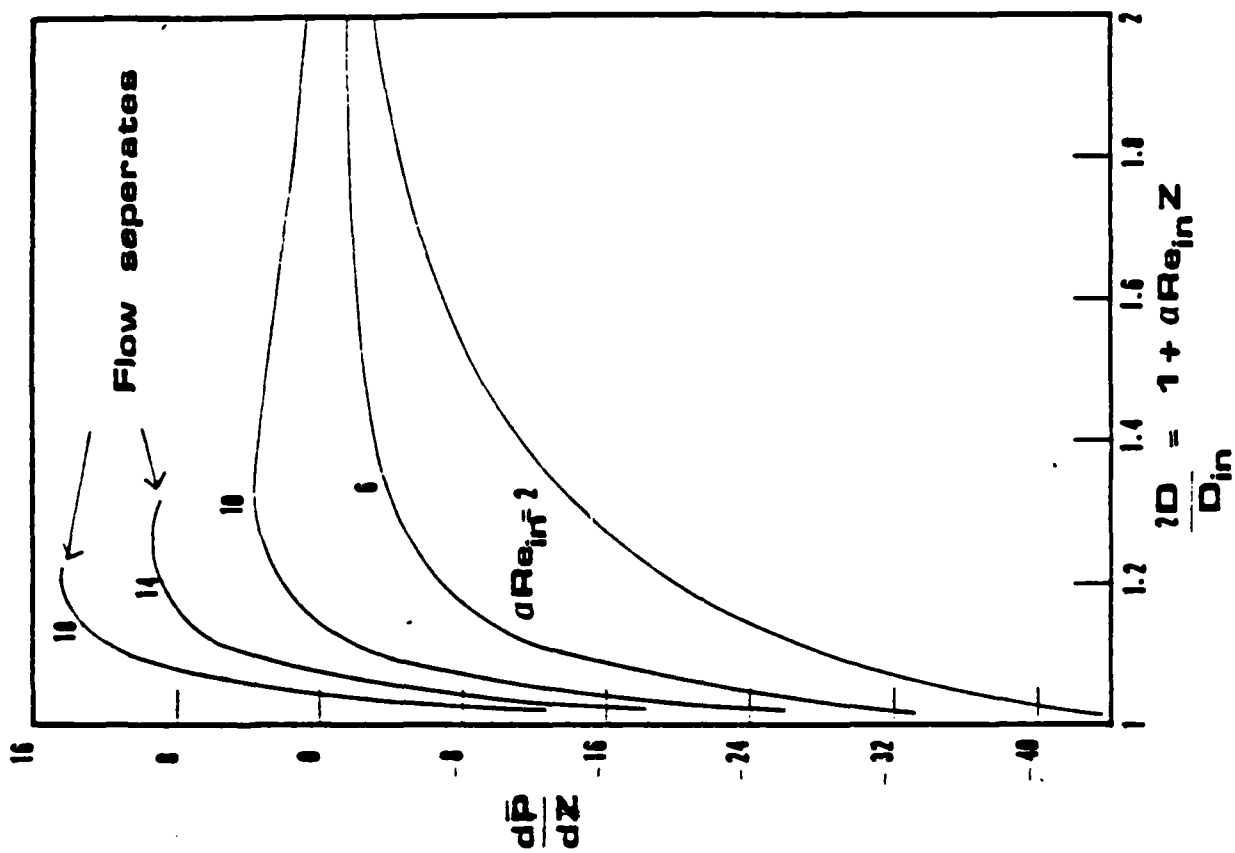


Fig. 5.10(6) Variation of the pressure gradient without source terms

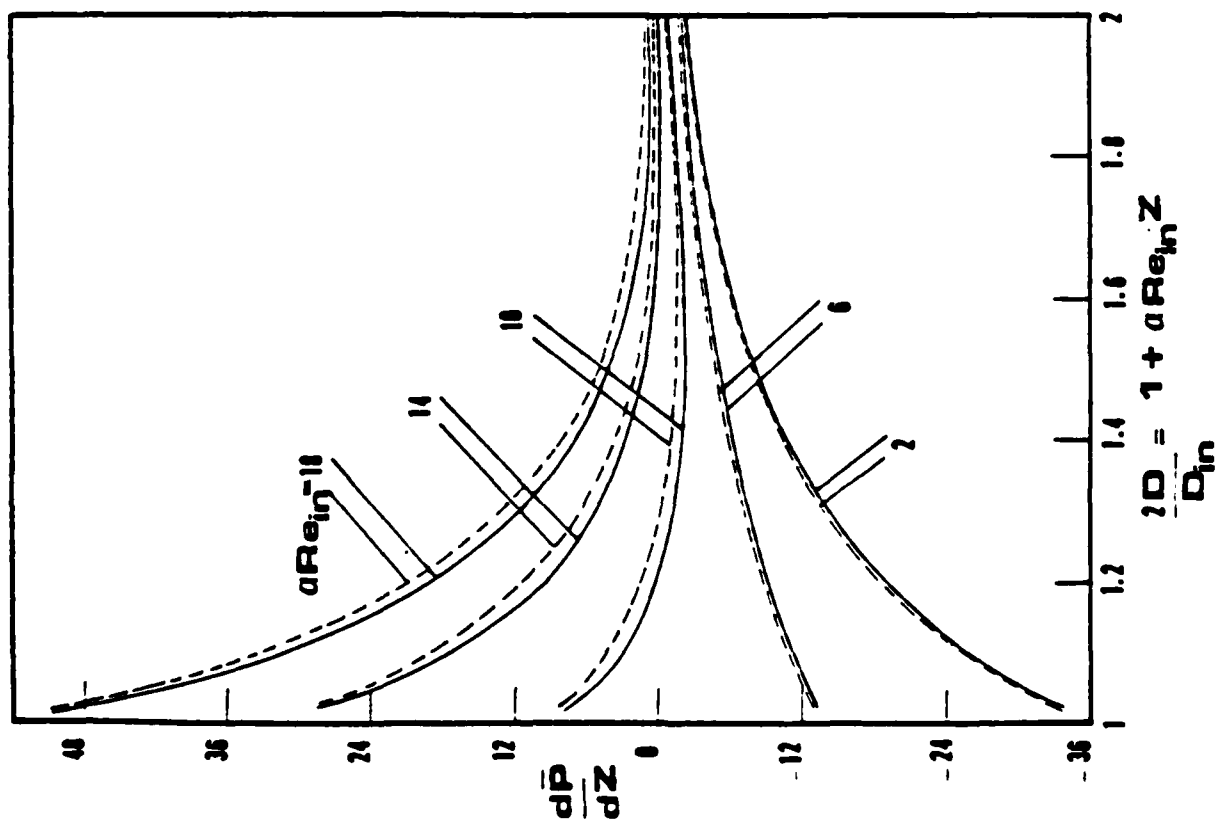


Fig. 5.10(a) Variation of the pressure gradient with source terms

Fig. 5.10(a) represent the exact solution; the agreement can be seen to be very good. For the flow without the extra source terms, separation is encountered for large angles of the diffuser.

The variation of centerline velocity with the axial distance Z is shown in Fig. 5.11. Once again, good agreement with the exact solution is seen in Fig. 5.11(a), while the flow separation in absence of the special source terms is evident in Fig. 5.11(b). The development of the axial velocity profiles for the case of zero source terms is shown in Fig. 5.12. The profiles at flow separation can be seen to exhibit an inflexion point at the wall.

5.2-3 Flow through an elliptic duct

For the flow through an elliptic duct, the following geometrical relations are used.

$$2D_x = D_{in} + \alpha z \quad (5.31)$$

$$2D_y = \frac{(D_{in}) \cdot (D_{in})}{(2D_x)} \quad (5.32)$$

$$D_0 = D_{in}/2 \quad (5.33)$$

$$\gamma = \alpha/2 \quad (5.34)$$

$$D_x = D_0 + \gamma z \quad (5.35)$$

$$D_y = D_0^2/D_x \quad (5.36)$$

Thus, at the inlet, the cross section of the duct is a circle of diameter D_{in} (radius $D_0 = D_{in}/2$).

Because of symmetry, only one quarter of the duct needs to be considered. A cross section of the quarter of the duct, and its discretization into triangular elements is shown in Fig. 5.13. A 17 x 17 grid is used.

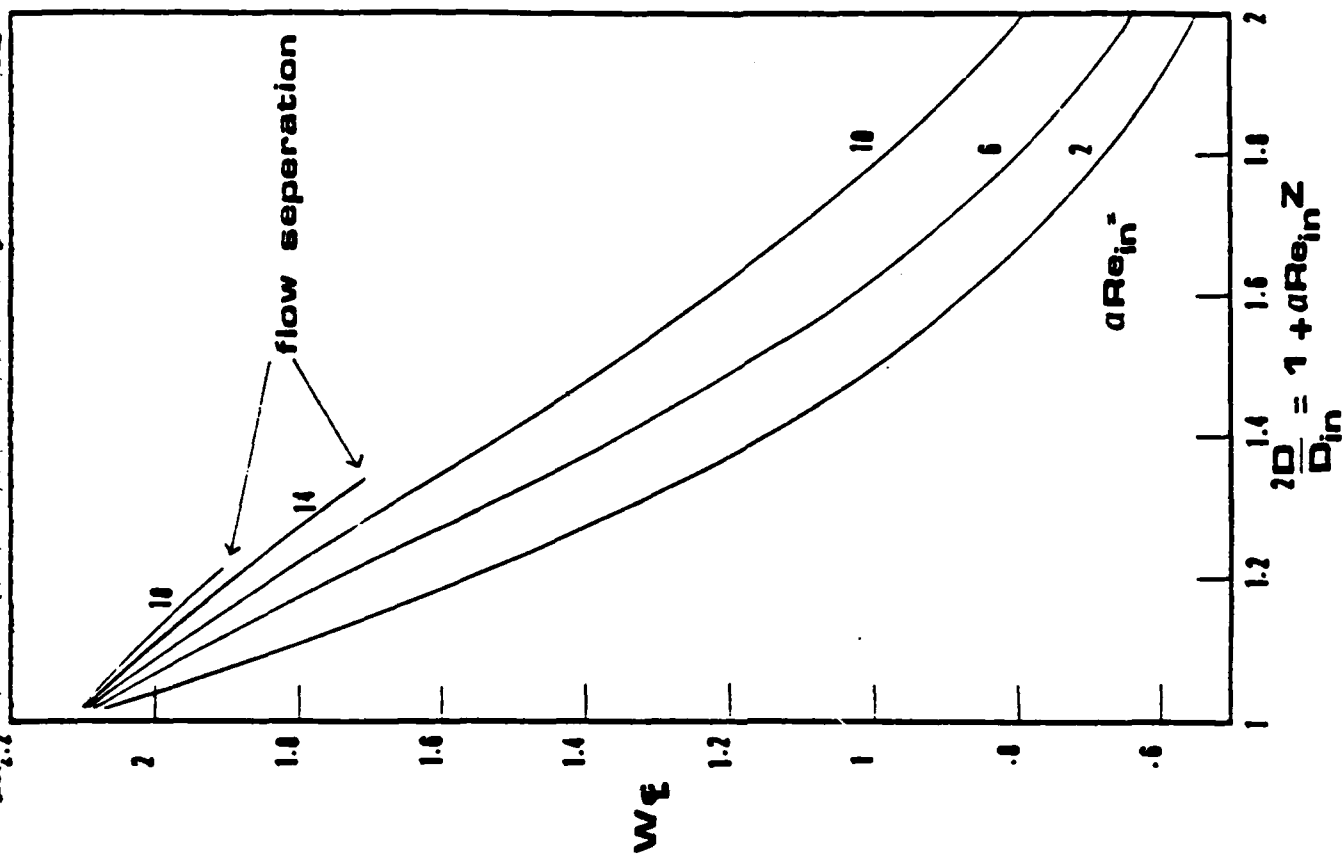


Fig. 5.11(b) Decay of centerline velocity without source terms

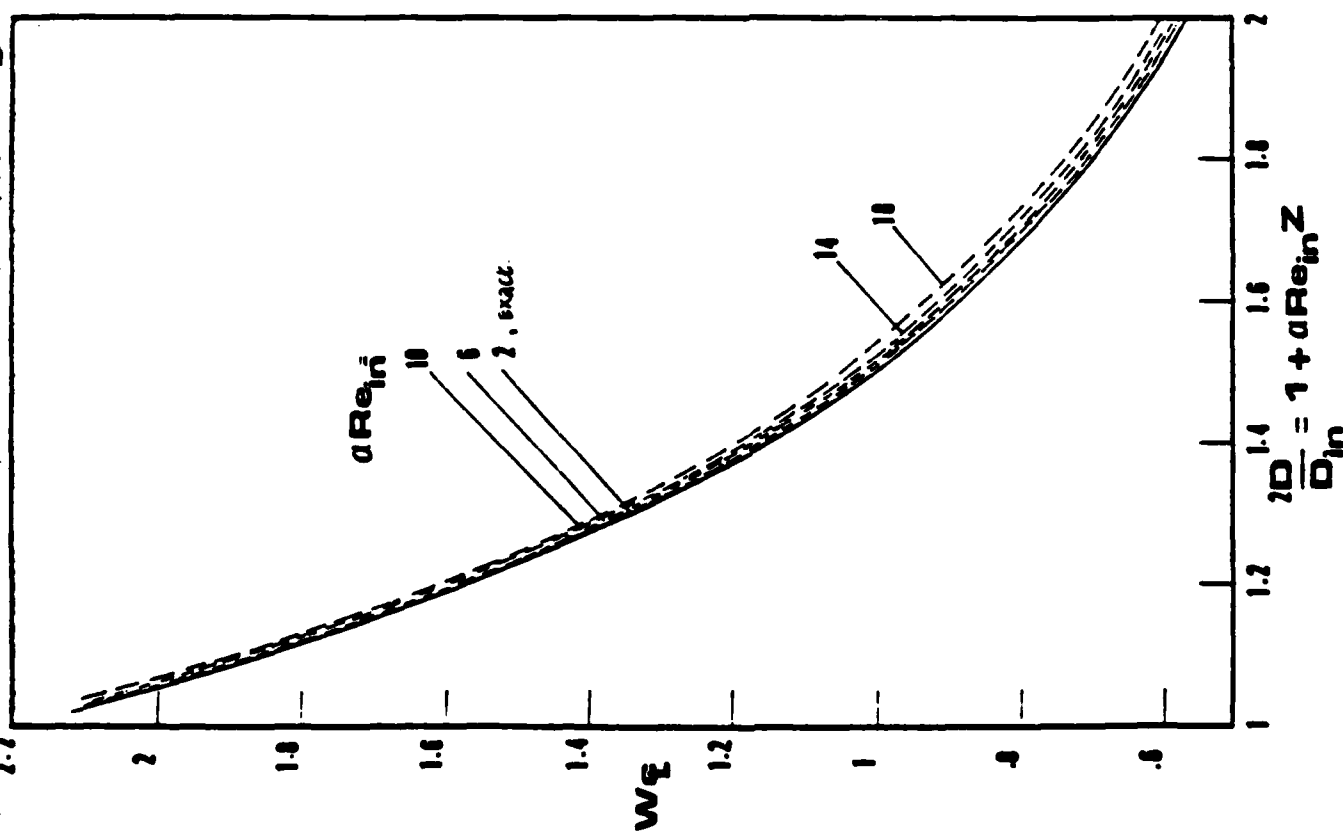


Fig. 5.11(a) Decay of centerline velocity with source terms

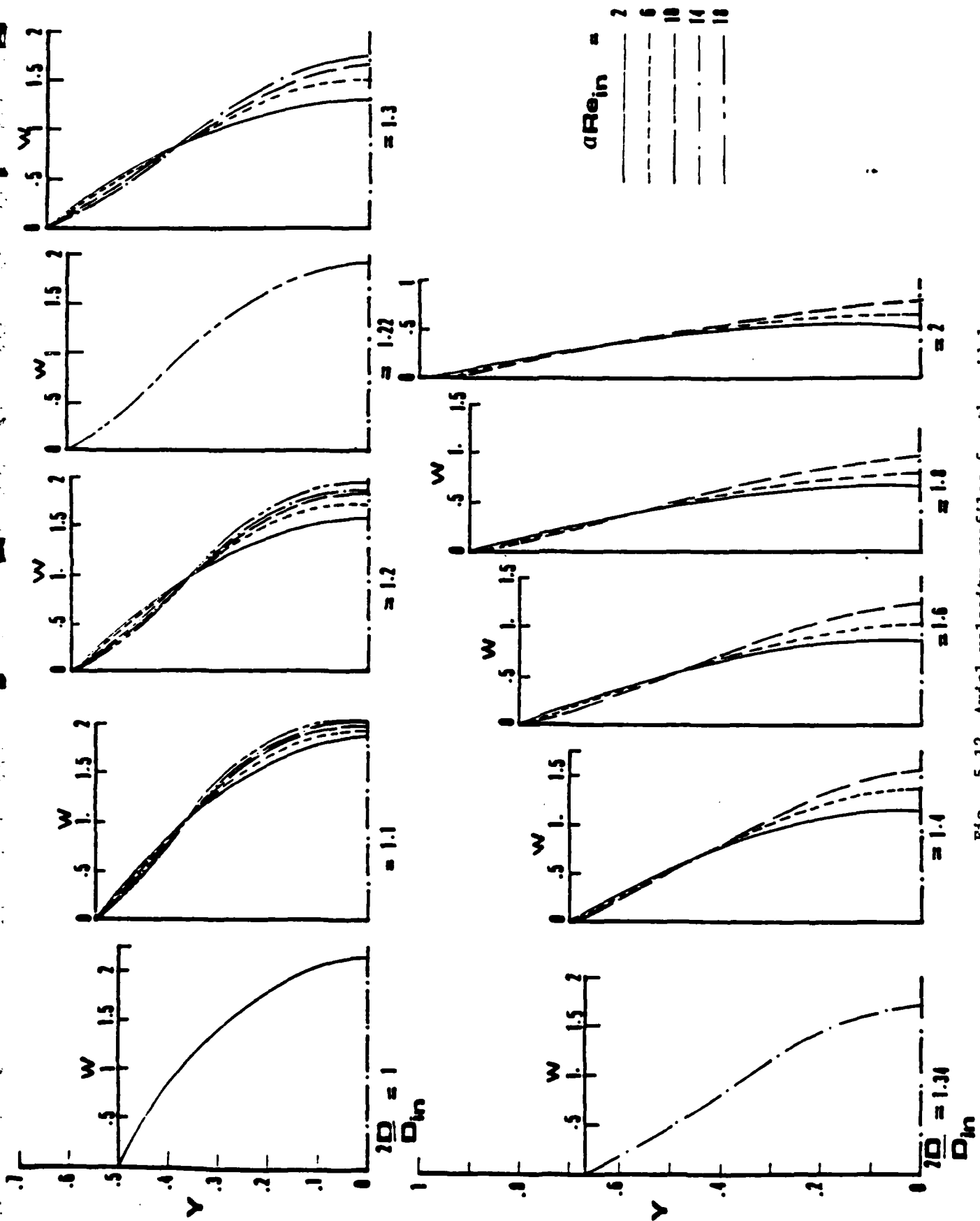


Fig. 5.12 Axial velocity profiles for the midplane

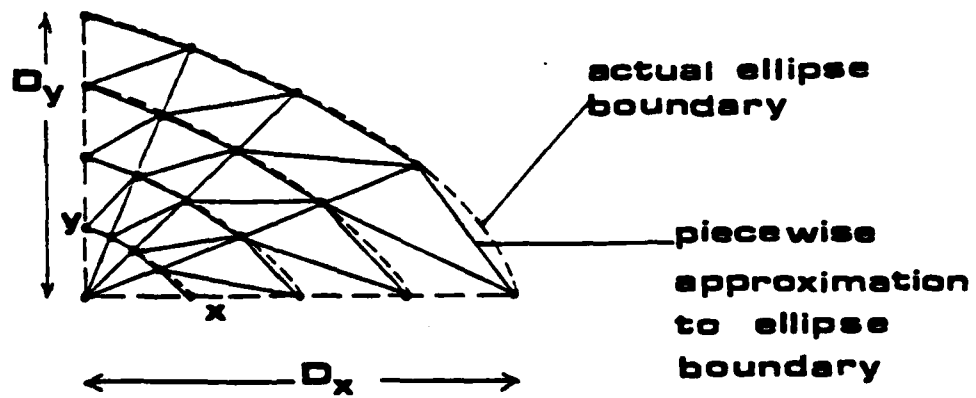


Fig. 5.13 Discretization for the elliptic duct

The variation of dimensionless axial pressure gradient $d\bar{P}/dZ$ with the axial distance Z is shown in Fig. 5.14 for a range of values αRe_{in} . The results for the flow with source terms are displayed in Fig. 5.14(a) and the results without the source terms are shown in Fig. 5.14(b). It is evident from Fig. 5.14(a) that the computed results are in good agreement with the exact solution even for large values of αRe_{in} .

The variation of axial velocity (w/\bar{w}_{in}) on the semi-major and semi-minor axes of the ellipse for the flow with source terms is shown in Fig. 5.15. Also shown is the exact solution. The agreement between the computed and exact velocity profiles can be seen to be very good. The velocity profiles for the flow without source terms are shown in Fig. 5.16.

6. Concluding remarks

This report has described the development of a calculation procedure for three-dimensional flow in ducts of varying cross sections. The procedure is developed in two stages. First, a calculation scheme for two-dimensional flows is described. Then, it is used as the solution method over a cross section of a duct in a marching procedure. Examples of both two-dimensional flows and three-dimensional duct flows are provided to demonstrate the capabilities of the proposed procedure.

Further work in this research project consists of additional testing of the method and the development of partially parabolic and fully elliptic procedures for more complex duct flows.

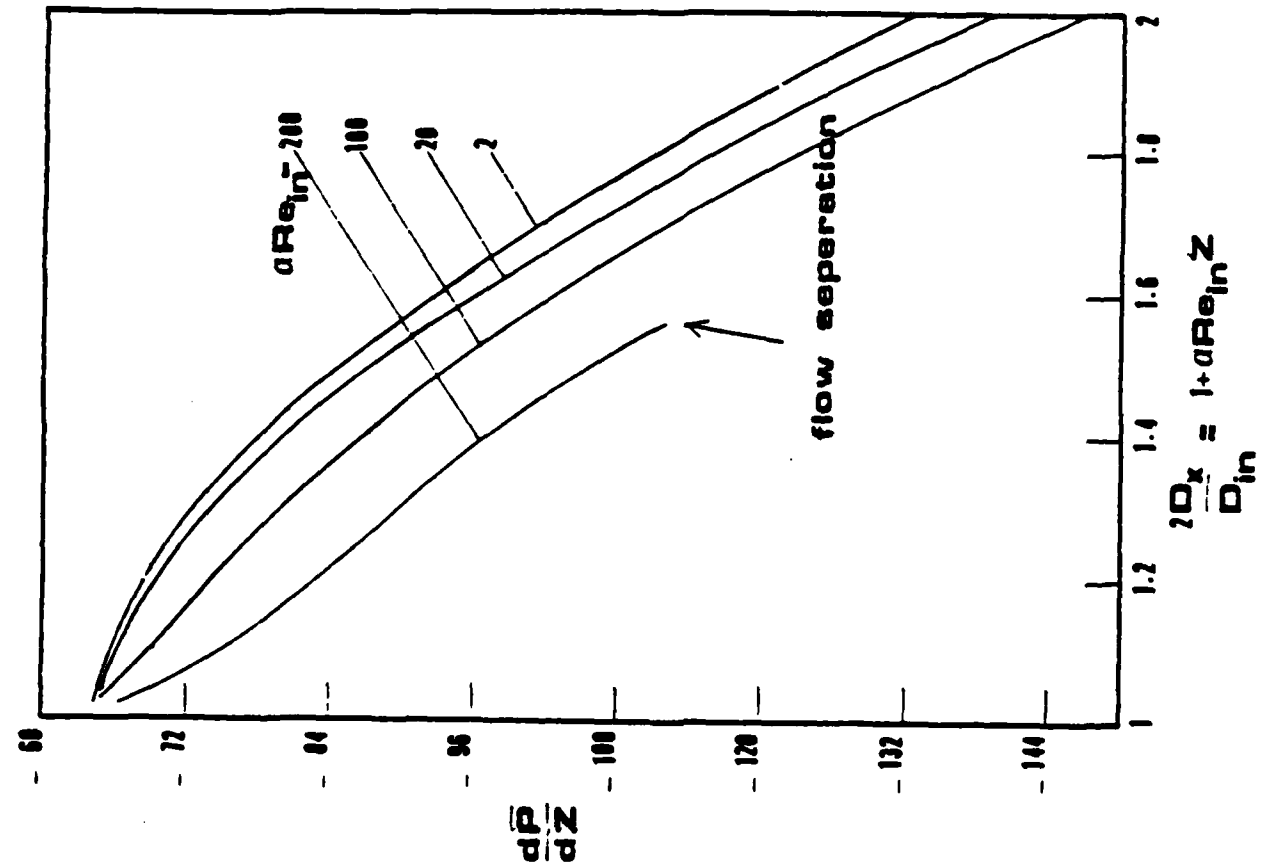


Fig. 5.14(b) Variation of the pressure gradient without source terms

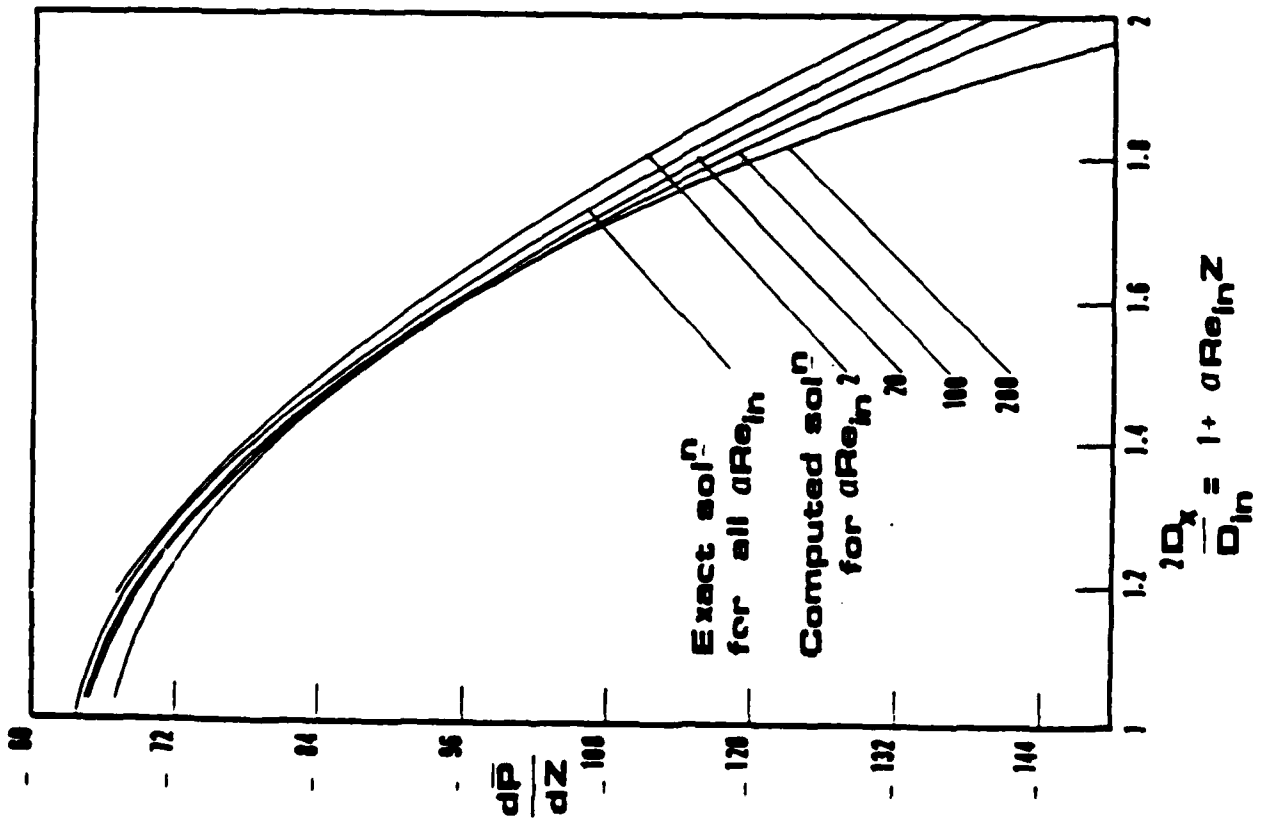


Fig. 5.14(a) Variation of the pressure gradient with source terms

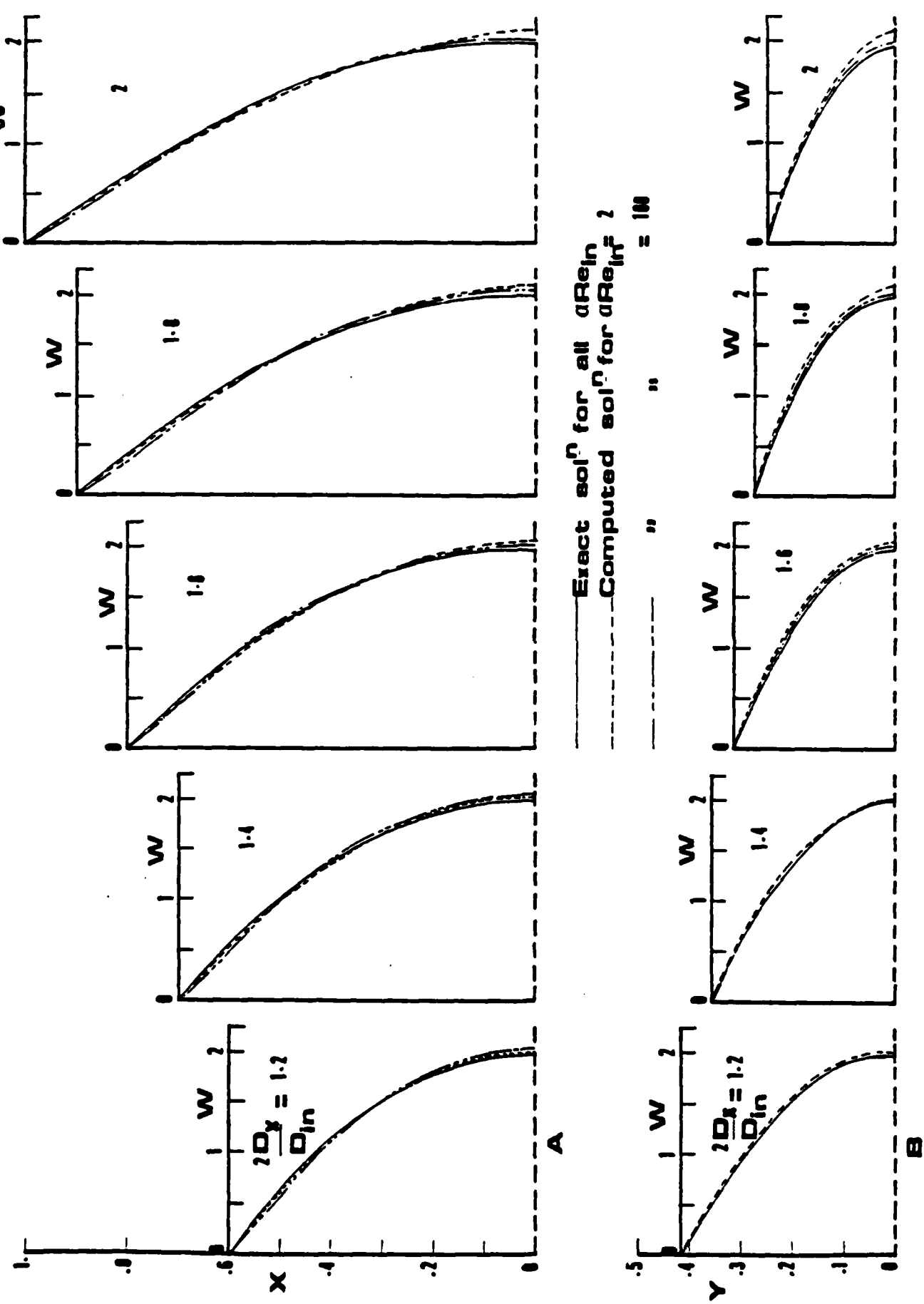


Fig. 5.15 Velocity profiles with source terms

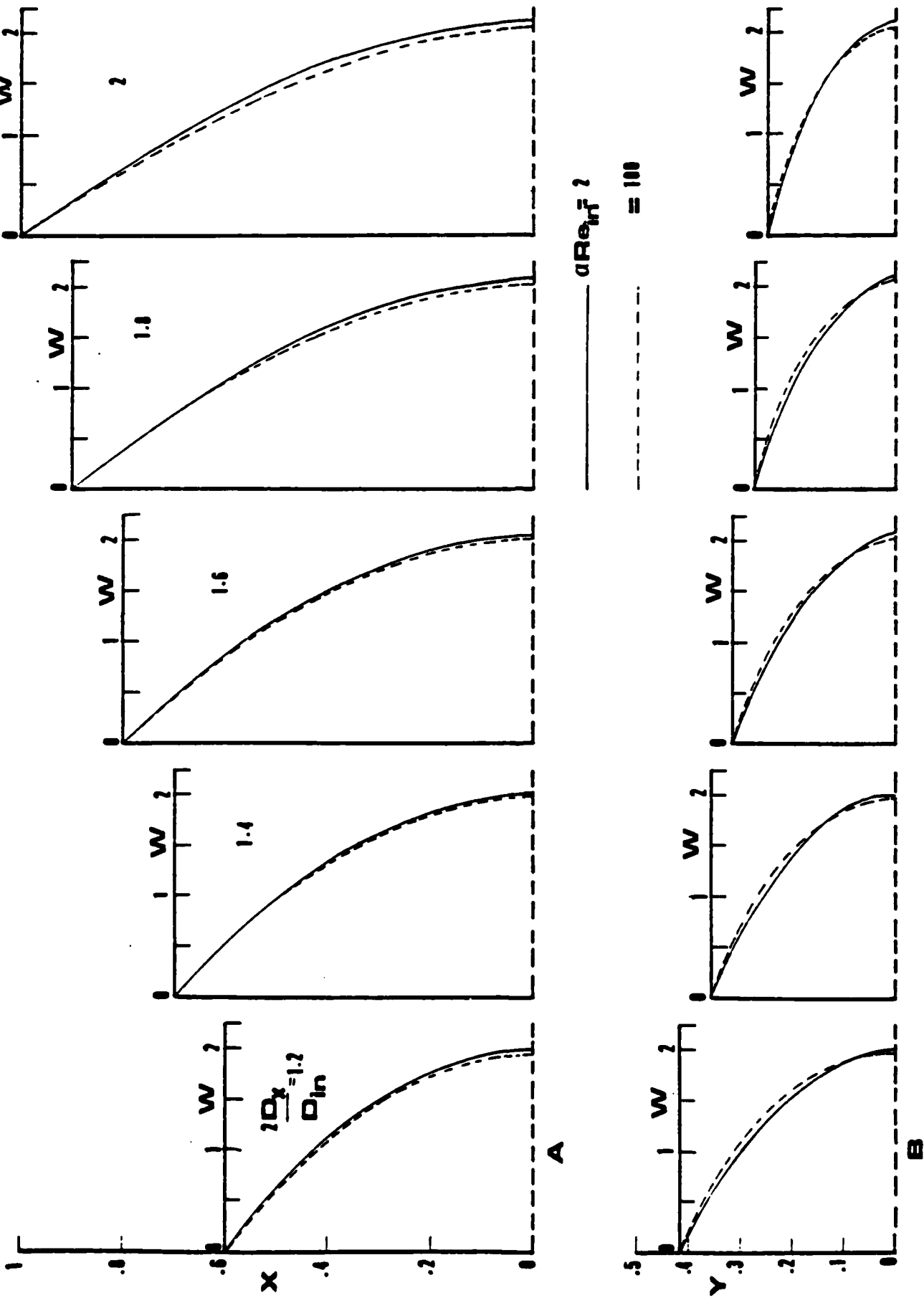


Fig. 5.16 Velocity profiles without source terms

References

1. Baliga, B. R. and Patankar, S. V. "A new finite element formulation for convection-diffusion problems" Numer. Heat Transfer, Vol. 3, pp. 393-410, 1980.
2. Baliga, B. R. and Patankar, S. V. "A control-volume finite element method for two-dimensional fluid flow and heat transfer", Numer. Heat Transfer, Vol. 6, 1983.
3. Patankar, S. V. Numerical Heat Transfer and Fluid Flow, McGraw-Hill--Hemisphere, New York, 1980.
4. Burgraff, O. R. "Analytical and numerical studies of the structure of steady separated flows", J. Fluid Mech., Vol. 24, Part 1, pp. 113-151, 1966.
5. Raithby, G. D. and Schneider, G. E. "Numerical solution of problems in incompressible fluid flow: treatment of the velocity-pressure coupling", Numer. Heat Transfer, Vol. 2, pp. 417-440, 1979.
6. Beavers, G. S., Sparrow, E. M., and Magnuson, R. A. "Experiments on hydrodynamically developing flow in rectangular ducts of arbitrary aspect ratio", Int. J. Heat Mass Transfer, Vol. 13, pp. 689-702, 1970.
7. Goldstein, R. J. and Kreid, D. K. "Measurement of laminar flow development in a square duct using a Laser-Doppler flowmeter", J. Appl. Mech., Vol. 89, pp. 813-818, 1967.
8. Sparrow, E. M. and Loeffler, A. L. "Longitudinal laminar flow between cylinders arranged in regular array", AIChE Journal, Vol. 5, No. 3, pp. 325-330, 1959.

DISTRIBUTION LIST

HEAT TRANSFER

One Copy except
as noted

Mr. M. Keith Ellingsworth
Mechanics Division
Office of Naval Research
800 N. Quincy Street
Arlington, VA 22203

2

Defense Documentation Center
Building 5, Cameron Station
Alexandria, VA 22314

12

Technical Information Division
Naval Research Laboratory
4555 Overlook Avenue SW
Washington, DC 20375

6

Professor Paul Marto
Department of Mechanical Engineering
U.S. Naval Post Graduate School
Monterey, CA 93940

Professor Bruce Rankin
Naval Systems Engineering
US Naval Academy
Annapolis, MD 21402

Mr. Doug Marron
Code 05R13
Crystal Plaza # 6
Naval Sea Systems Command
Washington, DC 20362

Steam Generators Branch, Code 5222
National Center #4
Naval Sea Systems Command
Washington, D.C. 20362

Heat Exchanger Branch, Code 5223
National Center #3
Naval Sea Systems Command
Washington, D.C. 20362

Mr. Ed Ruggiero, NAVSEA 08
National Center #2
Washington, D.C. 20362

Dr. Earl Quandt Jr., Code 272
David Taylor Naval Ship R&D Center
Annapolis, MD 21402

Mr. Wayne Adamson, Code 2722
David Taylor Naval Ship R&D Center
Annapolis, MD 21302

Dr. Win Aung
Heat Transfer Program
National Science Foundation
Washington, DC 20550

Mr. Michael Perlsweig
Department of Energy
Mail Station E-178
Washington, DC 20545

Dr. W.H. Theilbahr
Chief, Energy Conservation Branch
Dept. of Energy, Idaho Operations Office
550 Second Street
Idaho Falls, Idaho 83401

Professor Ephriam M. Sparrow
Department of Mechanical Engineering
University of Minnesota
Minneapolis, MN 55455

Professor S.V. Patankar
Department of Mechanical Engineering
University of Minnesota
Minneapolis, MN 55455

Professor Daryl Metzger
Chairman, Mechanical and
Energy Systems Engineering
Arizona State University
Tempe, AZ 85281

Professor Ronald So
Mechanical and Energy Systems
Engineering
Arizona State University
Tempe, AZ 85281

Professor J.A.C. Humphrey
Department of Mechanical Engineering
University of California, Berkeley
Berkeley, CA 94720

Professor Brain Launder
Thermodynamics and Fluid Mechanics Division
University of Manchester
Institute of Science & Technology
PO88 Sackville Street
Mandhester M601QD England

Professor Shi-Chune Yao
Department of Mechanical Engineering
Carnegie-Mellon University
Pittsburgh, PA 15213

Professor Charles B. Watkins
Chairman, Mechanical Engineering Department
Howard University
Washington, DC 20059

Professor Adrian Bejan
Department of Mechanical Engineering
University of Colorado
Boulder, CO 80309

Professor Donald M. McEligot
Department of Aerospace and Mechanical Engineering
Engineering Experiment Station
University of Arizona
Tucson, Arizona 85721

Professor Paul A. Libby
Department of Applied Mechanics and Engineering Sciences
University of California San Diego
Post Office Box 109
La Jolla, CA 92037

Professor C. Forbes Dewey, Jr.
Fluid Mechanics Laboratory
Massachusetts Institute of Technology
Cambridge, MA 02139

Professor William G. Characklis
Dept. of Civil Engineering and Engineering Mechanics
Montana State University
Bozeman, MT 59717

Professor Ralph Webb
Department of Mechanical Engineering
Pennsylvania State University
208 Mechanical Engineering Bldg.
University Park, PA 16802

Professor Warren Rohsenow
Mechanical Engineering Department
Massachusetts Institute of Technology
77 Massachusetts Avenue
Cambridge, MASS 02139

Professor A. Louis London
Mechanical Engineering Department
Bldg. 500, Room 501B
Stanford University
Stanford, CA 94305

Professor James G. Knudsen
Associate Dean, School of Engineering
Oregon State University
219 Covell Hall
Corvallis, Oregon 97331

Professor Arthur E. Bergles
Mechanical Engineering Department
Iowa State University
Ames, Iowa 50011

Professor Kenneth J. Bell
School of Chemical Engineering
Oklahoma State University
Stillwater, Oklahoma 74074

Dr. James Lorenz
Componebt Technology Division
Argonne National Laboratory
9700 South Cass Avenue
Argonne, Illinois 60439

Dr. David M. Eissenberg
Oak Ridge National Laboratory
P.O. Box Y, Bldg. 9204-1, MS-0
Oak Ridge, Tennessee 37830

Dr. Jerry Taborek
Technical Director
Heat Transfer Research Institute
1000 South Fremont Avenue
Alhambra, CA 91802

Dr. Simion Kuo
Chief, Energy Systems
Energy Research Laboratory
United Technology Research Center
East Hartford, CT 06108

Mr. Jack Yampolsky
General Atomic Company
P.O. Box 81608
San Diego, CA 92138

Mr. Ted Carnavos
Noranda Metal Industries, Inc.
Prospect Drive
Newton, CONN 06470

Dr. Ramesh K. Shah
Harrison Radiator Division
General Motors Corporation
Lockport, New York 14094

Dr. Ravi K. Sakhuja
Manager, Advanced Programs
Thermo Electron Corporation
101 First Avenue
Waltham, MASS 02154

Mr. Robert W. Perkins
Turbotec Products, Inc.
533 Downey Drive
New Britain, CONN 06051

Dr. Keith E. Starner
York Division, Borg-Warner Corp.
P.O. Box 1592
York, PA 17405

Mr. Peter Wishart
C-E Power Systems
Combustion Engineering, Inc.
Windsor, CONN 06095

Mr. Henry W. Braum
Manager, Condenser Engineering Department
Delaval
Front Street
Florence, New Jersey 08518

Dr. Thomas Rabas
Steam Turbine-Generator Technical Operations Division
Westinghouse Electric Corporation
Lester Branch
P.O. Box 9175 N2
Philadelphia, PA 19113

END

FILMED

8-83

DTIC